Research article

Turing patterns in a 3D morpho-chemical bulk-surface reaction-diffusion system for battery modeling[†]

Massimo Frittelli[1,*]**, Ivonne Sgura**[1] **and Benedetto Bozzini**[2]

[1] Department of Mathematics and Physics "E. De Giorgi", University of Salento, Lecce 73100, Italy

[2] Department of Energy, Politecnico di Milano, Milano 20156, Italy

[†] **This contribution is part of the Special Issue:** Advancements in Polytopal Element Methods
  Guest Editors: Michele Botti; Franco Dassi; Lorenzo Mascotto; Ilario Mazzieri
  Link: `www.aimspress.com/mine/article/6538/special-articles`

* **Correspondence:** Email: massimo.frittelli@unisalento.it.

Abstract: In this paper we introduce a bulk-surface reaction-diffusion (BS-RD) model in three space dimensions (3D) that extends the so-called DIB morphochemical model to account for the electrolyte contribution in the application, in order to study structure formation during discharge-charge processes in batteries. Here we propose to approximate the model by the bulk-surface virtual element method (BS-VEM) on a tailor-made mesh that proves to be competitive with fast bespoke methods for PDEs on Cartesian grids. We present a selection of numerical simulations that accurately match the classical morphologies found in experiments. Finally, we compare the Turing patterns obtained by the coupled 3D BS-RD model with those obtained with the original 2D version.

Keywords: batteries; metal electrode; electrodeposition; bulk-surface reaction-diffusion systems; bulk-surface virtual element method; Turing patterns

1. Introduction

The formation of spatio-temporal structures in electrodeposition is a relevant physical phenomenon, as it impacts several applications, ranging from the durability and efficiency of batteries to electroplating [1]. The onset of spatio-temporal structures on the cathodic surface was proven to be initiated by a Turing morphogenetic mechanism, where the physics are modeled by a suitable reaction-diffusion system (RDS), called DIB model after the authors [1, 2], whose spatial domain is the electrodic surface. In the DIB model, the spatial domain is assumed to be fixed and does not change over time, as the growth/corrosion effects are fully modeled by the dynamics of the system.

By tweaking the parameters of the DIB model, it is possible to successfully simulate spatial [1] or spatio-temporal patterns [2] of various morphological classes that are experimentally observed under appropriate physical and chemical conditions; these include spatial patterns such as spots, holes, stripes, labyrinths, and spiral waves. The effectiveness of the DIB model has justified the development of extensions and ameliorations, such as the introduction of cross-diffusion [3] and the generalization of the spatial domain to be a curved surface [4, 5].

As it stands, one of the limitations of the DIB model is that it does not fully accounts for the effects of non-uniform electrolyte concentration in a neighborhood of the electrode. Experimentally, such non uniform concentration is induced by the spatial structures arising on the electrode and, in turn, affects further structure development. In this regard, the electrode-electrolyte system has a two-way coupling that, in the long run, can drastically affect the resulting morphological class. In this paper we propose the *bulk-surface DIB (BS-DIB) model* in three space dimensions to fill this gap. In the proposed model, the surface represents the electrode (where the electrodeposition takes place), while the 3D bulk models the electrolyte. The physical two-way coupling mentioned above causes the proposed model to take the form of a *coupled bulk-surface reaction-diffusion system (BS-RDS)* [6–8].

For domains of general shape, different numerical methods were developed for the spatial approximation of BS-RDSs, such as the Bulk-Surface Finite Element Method (BS-FEM) [7], the Cut Finite Element Method [9], unfitted finite element methods [10], and meshless kernel methods [11], just to mention a few. In all of these methods, the spatially discrete problem takes the form of a large ODE system, whose dimension is equal to the number of spatial degrees of freedom. Thus, the high level of spatial resolution required by RDSs and BS-RDSs, together with the curse of dimensionality (3D), makes the numerical approximation of the BS-DIB model a challenging computational task. In the present context, where the bulk domain is a cube, a bespoke tensorized technique called Matrix-Oriented Finite Element Method (MO-FEM) [12, 13] can be exploited to take advantage of the special geometry and drastically reduce the computational execution times. However, it is worth noting that the BS-DIB model can exhibit spatial patterns only in a neighborhood of the surface, hence a uniform spatial discretization is computationally inefficient. For this reason, we exploit the geometric flexibility of the bulk-surface virtual element method (BS-VEM) [8] to adopt a graded cubic mesh that is highly refined close to the surface and much coarser away from the surface. Such a mesh is simultaneously graded and entirely composed of cubic-shaped elements. Such a combination entails the presence of hanging nodes and edges, that are naturally handled by the BS-VEM and are not admissible in the BS-FEM. Compared to the MO-FEM, we show that the BS-VEM on such mesh exhibits a much lower number of degrees of freedom on equal level of spatial refinement in a neighborhood of the surface, where high spatial accuracy is actually required and produces patterns of the same morphological class. It needs to be noted that Turing patterns are highly sensitive to initial conditions, which are bound to be different between MO-FEM ad BS-VEM since the spatial meshes are different, hence obtaining the same morphological class with both methods is a sensible benchmark.

We present a wide range of numerical simulations for both the 2D DIB and the 3D BS-DIB models on equal parameters, to showcase the effect of the bulk-surface coupling. From the experiments we draw the following conclusions. First, the BS-DIB model appears to have a larger Turing region in the parameter space compared to the DIB model. In fact, for several choices of the parameters outside the Turing region of the DIB model, only the BS-DIB model exhibits spatial patterns. Second, when the DIB model exhibits spatial patterns, the BS-DIB model still exhibits patterns, but of different

morphological class, thereby further highlighting the impact of the bulk-surface coupling. A rigorous analysis of the Turing instability for the BS-DIB model will be addressed in future work.

The structure of the paper is as follows. In Section 2 we introduce the BS-DIB model, we give its physical interpretation and we analyse the stability of a relevant spatially uniform equilibrium in the absence of diffusion. In Section 3, we recall from [14] the BS-VEM and we present a bespoke graded polyhedral mesh that allows the BS-VEM to outperform the MO-FEM when solving the BS-DIB model. In Section 4, we present an extensive list of numerical experiments that empirically demonstrate the effect of the bulk-surface coupling on pattern formation. Conclusions are drawn in Section 5.

2. The bulk-surface DIB model on the cube

In this section, we present for the first time the morpho-chemical bulk-surface DIB (BS-DIB) PDE system for battery modeling. For simplicity, we consider a cube Ω for the 3D bulk that represents the electrolyte, and its bottom face Γ as the surface representing the electrode where the electrodeposition process takes place, see Figure 1.
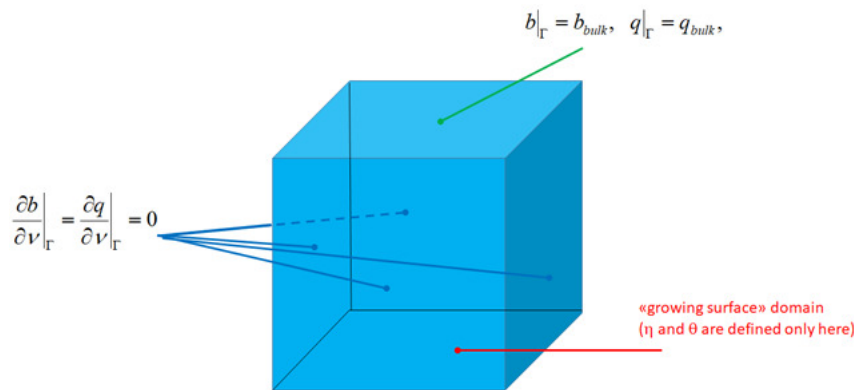

Figure 1. Bulk-surface DIB model: domain geometry and BCs for the bulk variables b, q.

Hence, let $\Omega = [0, L]^3$ be a cube of edge $L > 0$, let $\Gamma := [0, L]^2 \times \{0\}$ be the bottom face of Ω, let $\Gamma_T = [0, L]^2 \times \{L\}$ be the top face of Ω and let $\Gamma_L = \partial\Omega \setminus (\Gamma \cup \Gamma_T)$ be the union of the lateral faces of Ω. Let $T > 0$ be the final time. For the diffusion operators, Δ will indicate the 3D Laplace operator in Ω, while Δ_Γ the Laplace-Beltrami operator on Γ (which in this case coincides with the 2D Laplacian since Γ is flat). We recall that the morpho-chemical DIB-model has been originally introduced in [1] on a 2D rectangular spatial domain, say $Q \subset \mathbb{R}^2$, in the framework of reaction-diffusion PDEs, with the original feature of coupling one equation for the morphology $\eta(x, y, t)$ with one for the surface chemistry $\theta(x, y, t)$, and takes the form:

$$\begin{cases} \dot{\eta} - \Delta_\Gamma \eta = f(\eta, \theta) & \text{in } Q; \\ \dot{\theta} - d_\theta \Delta_\Gamma \theta = g(\eta, \theta) & \text{in } Q; \\ \nabla\eta \cdot \mathbf{n} = 0, \qquad \nabla\theta \cdot \mathbf{n} = 0 & \text{on } \partial Q; \\ \eta(\mathbf{x}, 0) = \eta_0(\mathbf{x}), \qquad \theta(\mathbf{x}, 0) = \theta_0(\mathbf{x}) & \text{in } Q, \end{cases} \tag{2.1}$$

where $\mathbf{n} : \partial Q \to \mathbb{R}^2$ is the outward unit normal vector on ∂Q. Essentially, here we consider that this system *lives* on the bottom face of the cube, i.e., $Q \equiv \Gamma$ and suitable modifications of the source terms are needed to describe the new physico-chemical features, as explained in the following. Concerning the unknown variables, also here we suppose that on the (flat) surface Γ, $\eta \in \mathbb{R}$ expresses the instantaneous increment of the electrodeposit thickness during an electrochemical process and $\theta \in [0, 1]$ is the surface coverage with an adsorbed chemical species, that influences the electrodepostion and corrosion processes. In the last ten years several theoretical and numerical results have been published on the 2D-DIB model (2.1), as reported in the Introduction and in the bibliography. Moreover, a wide range of experimental demonstrations of electrochemical pattern formation, has been documented. In most of the papers, the existence of the so-called Turing patterns has been proved theoretically, demostrated by numerical simulations and validated through comparison with experiments, also in the case of 3D surfaces (see [4]). Hence, to account for the more realistic presence of the battery electrolyte, the bulk-surface (BS)-DIB model seeks to find four functions: $b, q : \Omega \times [0, T] \to \mathbb{R}$ in the bulk and $\eta, \theta : \Gamma \times [0, T] \to \mathbb{R}$ on the surface that fulfil the following systems of PDEs:

$$\begin{cases} \dot{b} - \Delta b = f_1(b) & \text{in } \Omega; \\ \dot{q} - d_\Omega \Delta q = f_2(q) & \text{in } \Omega; \end{cases} \tag{2.2a}$$

$$\begin{cases} \dot{\eta} - \Delta_\Gamma \eta = f_3(b, \eta, \theta) & \text{on } \Gamma; \\ \dot{\theta} - d_\Gamma \Delta_\Gamma \theta = f_4(q, \eta, \theta) & \text{on } \Gamma, \end{cases} \tag{2.2b}$$

and are coupled through the boundary conditions (BCs) for the bulk variables b and q given by

$$\begin{cases} \nabla b \cdot \mathbf{n} = -f_3(b, \eta, \theta)\psi_\eta & \text{on } \Gamma; \\ \nabla q \cdot \mathbf{n} = -f_4(q, \eta, \theta)\psi_\theta & \text{on } \Gamma; \\ \nabla b \cdot \mathbf{n} = 0, \quad \nabla q \cdot \mathbf{n} = 0, & \text{on } \Gamma_L; \\ b = b_0, \quad q = q_0, & \text{on } \Gamma_T. \end{cases} \tag{2.3}$$

Moreover, zero Neumann BCs for (2.2b) for the surface variables η and θ are considered, inherited by the original 2D-DIB model (2.1)

$$\begin{cases} \nabla \eta \cdot \mathbf{n} = 0 & \text{on } \partial\Gamma; \\ \nabla \theta \cdot \mathbf{n} = 0 & \text{on } \partial\Gamma. \end{cases} \tag{2.4}$$

The initial conditions are prescribed by:

$$b(\mathbf{x}, 0) = b_0 \in \mathbb{R}; \qquad q(\mathbf{x}, 0) = q_0 \in \mathbb{R}; \qquad \eta(\mathbf{x}, 0) = \eta_0(\mathbf{x}); \qquad \theta(\mathbf{x}, 0) = \theta_0(\mathbf{x}), \quad \mathbf{x} \in \Omega. \tag{2.5}$$

In (2.2), $d_\Omega > 0$ and $d_\Gamma > 0$ are adimensional diffusion coefficients. It is worth noting that the constants $\psi_\eta \geq 0$ and $\psi_\theta \geq 0$ are responsible of the strength of the BS coupling, in fact when they are equal to zero the two systems in (2.2) will be independent and the 2D DIB model (2.1) must be recovered by Eqs (2.2b)–(2.4).

In the bulk Eq (2.2a), $b(\mathbf{x}, t)$ represents the concentration of the electroactive cations (precursors of metal that is electrodeposited during the recharge cycle of the battery), present exclusively in the bulk and $q(\mathbf{x}, t)$ represents the bulk concentration of an additive species that is adsorbed at the cathode

as a way of controlling shape change with the coverage degree expressed by the variable θ in (2.2b). Concerning the source terms for the bulk species b and q, the kinetics f_1, f_2 are defined by:

$$f_1(b) := -k_b(b - b_0); \tag{2.6}$$

$$f_2(q) := -k_q(q - q_0); \tag{2.7}$$

where $b_0 = b_{bulk} \in \mathbb{R}$ and $q_0 = q_{bulk} \in \mathbb{R}$, represent the "bulk concentrations" and $k_b, k_q \geq 0$ are reaction rates.

For the surface variables η and θ, in (2.2b) the kinetics f_3 and f_4 are defined by:

$$f_3(b, \eta, \theta) := \rho \left[b_{|\Gamma} \cdot A_1(1 - \theta)\eta - A_2\eta^3 - B(\theta - \alpha) \right]; \tag{2.8}$$

$$f_4(q, \eta, \theta) := \rho \left[q_{|\Gamma} \cdot C(1 + k_2\eta)(1 - \theta)(1 - \gamma(1 - \theta)) - D(1 + k_3\eta)\theta(1 + \gamma\theta) \right], \tag{2.9}$$

and correspond to the source terms of the DIB model (2.1), but this time including the bulk contributions, as described in details below and such that

$$f(\eta, \theta) = f_3(1, \eta, \theta); \quad g(\eta, \theta) = f_4(1, \eta, \theta),$$

see [1]. In (2.6)–(2.9), the model parameters $k_b, k_q, k_2, k_3, \rho, \alpha, A_1, A_2, B, C, D$ are positive constants, and $\gamma \geq 0$.

2.1. Physical meaning of source terms

In the kinetics f_1, f_2:

- $b_0 = b_{bulk} \in \mathbb{R}$ and $q_0 = q_{bulk} \in \mathbb{R}$, represent the "bulk concentrations", that prevail at equilibrium, when the bulk is homogeneous. The physical meaning of the terms $(b - b_0)$ and $(q - q_0)$, with $k_b, k_q \geq 0$ is first-order homogeneous reaction kinetics describing the tendency of the reagent to re-establish the equilibrium concentration. This can be considered a very simple model of a situation in which b, q are the concentrations of the species involved in the electrodic reaction in the electroactive form, that is generated by the decomposition of some precursor (e.g., metallic ion with a ligand that keeps the ion in solution in non-electroactive form, from which the electroactive species forms by decomposition of the complexed one). A *lower-than-equilibrium* local concentration of b, q (e.g., by cathodic consumption) generates new b, q (by decomposition of the complexed form); while a *higher-than-equilibrium* concentration (e.g., by anodic injection) generates a consumption (e.g., by reaction with the ligand, yielding the non-electroactive form).

For aim of completeness, here we recall and update the meaning of the kinetics of the DIB modeling (i.e., f, g, f_3, f_4). The physical meaning of the terms in f_3 in (2.8) can be described as follows:

- As in [1], the Butler-Volmer type electrokinetic term $A_1(1 - \theta)\eta$ is the charge-transfer rate at sites free from adsorbates, but *here* this is scaled by the concentration of the electroactive species at the surface $b_{|\Gamma}$. This corresponds to first-order phenomenological kinetics and it includes naturally mass-trasport effects from the bulk to the surface (i.e., the mass-transport of the electroactive species b present in the bulk and reacting electrochemically at the surface).

- The cubic term $-A_2\eta^3$ in the original DIB model [1] represents collectively all "hindrances" to η (growth) resulting from "the establishment of high values of η". The most straightforward interpretation of such hindrances is mass-transport limitation that–in a Gileadi-type framework– can be approximately accounted for with a negative cubic correction to the I-V curve. As expounded above, in the new bulk-surface context mass-transport limitations can be naturally accounted for by multiplying the term linear in η by the surface concentration $b_{|\Gamma}$ of the reactant b present in the bulk and describing the electroactive species. Nevertheless, in the bulk-surface version of DIB it is worth retaining the cubic term in η, because this can account for other hindrances to metal growth (i.e., beyond mass-transport from the bulk to the reactive surface) appearing at high metal plating rates, such as cathodic passivation.
- The term $-B(\theta - \alpha)$ quantifies the effect of adsorbates on the electrodeposition rate. The parameter $0 < \alpha \leq 1$ takes into account the fact that adsorbates can have both inhibiting and enhancing effects on the growth rate.
- Concerning the equation for the chemical coverage θ, in the original DIB model (2.1) the source term can be regarded as

$$g(\eta, \theta) = C\, g_{ads}(\eta, \theta) - D\, g_{des}(\eta, \theta)$$

and features adsorption (parameter C) and desorption (parameter D) terms including both chemical (expanded to second order) and electrochemical (first order) contributions. Here, the physical meaning of the modified kinetics f_4 in (2.2b) is that–coherently with the Langmuir adsorption model with monomolecular adsorption reaction–the adsorption term is directly proportional to the amount of the bulk species. In the case of a heterogeneous bulk phase, the relevant value of the bulk form is that in a neighborhood of the surface (commonly, referred to as the "catholyte") that is given by $q_{|\Gamma}$.

2.2. *Physical meaning of boundary conditions*

The coupling BCs for the bulk equations at the interface between the "growing surface Γ" and the "bulk Ω" can thus naturally be written as the first two equations in (2.3) indicating that the flux of bulk species to the surface is opposite to their consumption rates at the surface. More specifically, the physical meaning of the form of the first two equations in (2.3) is that, even though b and q coming from the bulk are consumed at the interface (i.e., in correspondence of their values $b_{|\Gamma}$ and $q_{|\Gamma}$) to yield η and θ only in a specific term of f_3 and f_4, the negative terms of these equations have the effect of injecting b and q into the bulk. Cases in which $\theta > \alpha$ (i.e., the adsorbate enhances electrodeposition, e.g., by resonant tunnelling effects), can be regarded as a special case of interfacial b consumption, accounted for through the BCs. Thus the net formation rate of η and θ is proportional to the fluxes of b and q to the surface.

$\nabla b \cdot \mathbf{n}, \nabla q \cdot \mathbf{n}$ denote the gradients normal to the boundary (surface) Γ, while ψ_η, ψ_θ are constants the role of which is to adjust the dimensionality of the equations and the physical meaning of which is explained below. ψ_η converts adatoms (i.e., the surface species generated by the consumption of b at the surface) into morphological units (the quantities actually described by η). Thus one can write: $\eta = \psi_\eta b$ and ψ_η can be regarded as a constant as far as the density of morphological units (ca. step) is proportional to the adatom density. ψ_θ expresses an isotherm, since it connects a bulk concentration (q) into a surface density (θ), hence, in as far as the isotherm can be linearised, we can write: $\theta = \psi_\theta q$.

To synthesize, the BCs for b and q in (2.3) are:

i) non-linear coupling BCs on the surface Γ, implying coupling with η and θ;

ii) Dirichlet BCs on the face of Ω opposite to Γ that is located far enough from the "bottom face" where reaction takes place, so that concentration gradients induced by reactivity have died out here;

iii) zero Neumann BCs (zero flux) on the residual faces of Ω (see Figure 1). The values of the bulk variables are thus set to their equilibrium values b_0, q_0 respectively.

For the morpho-chemical unknowns η and θ, the BCs for the 3D BS-DIB model on $\partial\Gamma$ are still zero Neumann BCs in (2.4).

2.3. Stability in the absence of diffusion

First of all, given the physical meaning of the BS-DIB model (2.2)-(2.3), it would make sense to consider spatial domains of more general shape. However, since the BS-DIB model is being introduced here for the first time, we have confined the presentation to the case of a cubic domain, in order to focus on the exploration of Turing patterns. A necessary condition to investigate diffusion-driven or Turing instability in the new BS model is that at least a homogeneous equilibrium of the PDE system exists and in the absence of diffusion it must be stable. In this section, we present this analysis, while the complete derivation of Turing conditions guaranteeing the existence of pattern formation in the presence of diffusion is deferred to another paper.

Hence, if $F = (f_1, f_2, f_3, f_4)$ accounts for all source terms involved and $\boldsymbol{\xi} = (b, q, \eta, \theta)^T$, it is easy to show that

$$F(\boldsymbol{\xi}^*) = 0 \quad \text{if} \quad \boldsymbol{\xi}^* = (b^*, q^*, \eta^*, \theta^*) = (b_0, q_0, 0, \alpha), \tag{2.10}$$

when in the BS-DIB model all parameters in (2.8)-(2.9) different from (B, C) are kept fixed after [2] as follows:

$$\begin{cases} k_2 = 2.5; \\ k_3 = 1.5; \\ \rho = 1; \\ \alpha = 0.5; \\ A_1 = 10; \\ D = q_0 \frac{C(1-\alpha)(1-\gamma+\gamma\alpha)}{\alpha(1+\gamma\alpha)}. \end{cases} \tag{2.11}$$

In fact, k_b, k_q do not influence the result in (2.10), (B, C) are still considered as bifurcation parameters as e.g., in [2] and the (η, θ) components of the equilibrium $\boldsymbol{\xi}^*$ coincide with the homogeneous equilibrium of the original 2D-DIB model. Here we analyze the stability of such equilibrium in the special case $\gamma = 0$, when the condition on the parameter D in (2.11) boils down to

$$\gamma = 0, \; D = q_0 \frac{C(1-\alpha)}{\alpha}. \tag{2.12}$$

To study the arising of the diffusion-driven or Turing instability in the BS-DIB model, it is necessary to prove that the equilibrium (2.10) is stable in absence of diffusion. In fact, the model (2.2), deprived of diffusion and linearized around the equilibrium in (2.10), is

$$\boldsymbol{\xi}_t = J(\boldsymbol{\xi}^*)(\boldsymbol{\xi} - \boldsymbol{\xi}^*), \tag{2.13}$$

where J is the Jacobian of the kinetics evaluated at the equilibrium (2.10). The matrix J has the following structure

$$J = \begin{pmatrix} J_\Omega & 0 \\ J_h & J_\Gamma \end{pmatrix}, \tag{2.14}$$

where, if $\gamma = 0$, the blocks of J are as follows:

$$J_\Omega := \begin{pmatrix} f_{1,b} & f_{1,q} \\ f_{2,b} & f_{2,q} \end{pmatrix} = \begin{pmatrix} -k_b & 0 \\ 0 & -k_q \end{pmatrix}; \tag{2.15}$$

$$J_h := \begin{pmatrix} f_{3,b} & f_{3,q} \\ f_{4,b} & f_{4,q} \end{pmatrix} = \rho \begin{pmatrix} A_1(1-\theta)\eta & 0 \\ 0 & C(1+k_2\eta)(1-\theta) \end{pmatrix}; \tag{2.16}$$

$$J_\Gamma := \begin{pmatrix} f_{3,\eta} & f_{3,\theta} \\ f_{4,\eta} & f_{4,\theta} \end{pmatrix} = \rho \begin{pmatrix} b_0 A_1(1-\alpha) & -B \\ q_0 C(k_2-k_3)(1-\alpha) & -\frac{q_0 C}{\alpha} \end{pmatrix}. \tag{2.17}$$

Thanks to the diagonal structure of J_Ω it holds that

$$\det(J - \lambda I) = (\lambda + k_b)(\lambda + k_q)\det(J_\Gamma - \lambda I). \tag{2.18}$$

It follows that two eigenvalues of J are $\lambda_1 = -k_b < 0$ and $\lambda_2 = -k_q < 0$. We are left to determine when the eigenvalues of J_Γ are negative. This happens if and only if $Trace J_\Gamma < 0$ and $\det J_\Gamma > 0$. Now:

$$Trace J_\Gamma = \rho\left(b_0 A_1(1-\alpha) - \frac{q_0 C}{\alpha}\right) < 0 \iff C > \frac{b_0}{q_0}A_1\alpha(1-\alpha), \tag{2.19}$$

and

$$\det J_\Gamma = \rho^2\left(BCq_0(k_2-k_3)(1-\alpha) - A_1 Cb_0 q_0 \frac{1-\alpha}{\alpha}\right) > 0 \iff B > \frac{A_1 b_0}{\alpha(k_2-k_3)}. \tag{2.20}$$

We obtain the following result.

Theorem 1. *If $\gamma = 0$, the equilibrium* (2.10) *is stable in the absence of diffusion if and only if*

$$B > \frac{A_1 b_0}{\alpha(k_2-k_3)} \qquad \wedge \qquad C > \frac{b_0}{q_0}A_1\alpha(1-\alpha). \tag{2.21}$$

In addition, if A_1, k_2, k_3, α are as in (2.11), *the condition* (2.21) *specializes to*

$$B > 20b_0 \qquad \wedge \qquad C > 2.5\frac{b_0}{q_0}. \tag{2.22}$$

Of course, as far as the conditions for Turing pattern formation are concerned, a specific study has to be carried out considering the full Jacobian J of Eq (2.14). This is an important study topic in its own right, that–nevertheless–has no impact on the analysis presented in this research. Since treating this problem exhaustively would be beyond the scope of the present work, we leave it to a subsequent publication.

Our present approach is to solve numerically the BS-DIB model for the diffusion coefficients $d_\Omega = 1$ and $d_\Gamma = 20$ and for a representative selection of parameter couples (B, C) generating the whole set of Turing pattern morphologies, as described in [15, 16]. In fact, this value of d_Γ was that used in [2, 15] to build a Turing region for the 2D-DIB model (2.1), that we will use as reference to investigate

numerically the Turing pattern formation for the new BS-DIB model (2.2). Moreover, we shall fix the model parameters in the bulk as

$$\begin{cases} b_0 = 1; & q_0 = 1; \\ k_b = 1; & k_q = 1; \end{cases} \tag{2.23}$$

such that such that the spatially homogeneous equilibrium for the system (2.2)-(2.3) is

$$\boldsymbol{\xi}^* = (b^*, q^*, \eta^*, \theta^*) = (1, 1, 0, \alpha), \tag{2.24}$$

that is stable in absence of diffusion if $B > 20$ and $C > 2.5$. To approximate Turing patterns as steady state solutions of the BS-DIB model, we choose the initial conditions as:

$$\begin{aligned} b(\mathbf{x}, 0) &= b_0; & q(\mathbf{x}, 0) &= q_0; \\ \eta(\mathbf{x}, 0) &= r_\eta(\mathbf{x}); & \theta(\mathbf{x}, 0) &= r_\theta(\mathbf{x}), \end{aligned} \tag{2.25}$$

where r_η and r_θ are random spatial data defined as

$$r_\eta(\mathbf{x}) = \eta^* + 1\text{e-}2 * \texttt{rand}(\mathbf{x}); \tag{2.26}$$

$$r_\theta(\mathbf{x}) = \theta^* + 1\text{e-}2 * \texttt{rand}(\mathbf{x}), \tag{2.27}$$

where η^* and θ^* are defined in (2.24) and $\texttt{rand}$ is the Matlab built-in function for generating uniform random numbers in $(0, 1)$.

In this scenario, our aim is to tune the coupling parameters ψ_η, ψ_θ to study from the numerical point of view the effect of coupling with the bulk on the morphological structure of the Turing patterns in the classes studied in [15]. We recall that the numerical approximation of RDSs in 3D is not straightforward because the pattern requires a very fine 3D mesh that provides sufficient spatial resolution and a long time integration to reach the asymptotic steady state. We shall apply the BS-VEM method studied in [8], for the space discretization of the 3D domain and surface and the IMEX Euler method as time solver. Hence, in the 3D case, if the cubic domain is approximated with a Cartesian grid, at least a million of unknowns at each time iteration are required. The usual implementation will thus end up to a sequence of linear systems where the coefficient matrix for each species is sparse, but prohibitively large. An efficient alternative to deal with this issue is the Matrix-Oriented Finite Element Method (MO-FEM) [12, 13] where, thanks to the Cartesian structure of the numerical grid, the fully discrete problem is transformed to a sequence of Sylvester matrix equations, that can be solved efficiently in the spectral space. However, since the BS-DIB model produces spatial patterns only in a neighborhood of the surface Γ, we devise a tailor-made graded polyhedral bulk-surface mesh where the BS-VEM proves to be a competitive alternative, since such a graded mesh avoids unnecessary refinement (and degrees of freedom) away from the surface Γ. One of the major advantages of this choice is that the BS-VEM, thanks to the flexibility of polyhedral meshes, can still be used on domains of general shape, where MO techniques might not apply.

3. The bulk surface virtual element method for the BS-DIB model

Formulating a BS-VEM [8] for the model (2.2) requires several steps. We start by rewriting the model (2.2) in such a way that the BCs lend themselves to a BS-VEM discretization.

3.1. Step 1: rewriting the model with homogeneous boundary conditions

In the presence of non-zero Dirichlet BCs, it is well-known [17] that it is first necessary to rewrite the PDE problem in such a way that the Dirichlet conditions are homogeneous. To this end, we define the following auxiliary variables and kinetics:

$$\widetilde{b} := b - b_0; \tag{3.1}$$

$$\widetilde{q} := q - q_0; \tag{3.2}$$

$$\widetilde{f_1}(\widetilde{b}) := f_1(\widetilde{b} + b_0); \tag{3.3}$$

$$\widetilde{f_2}(\widetilde{q}) := f_2(\widetilde{q} + q_0); \tag{3.4}$$

$$\widetilde{f_3}(\widetilde{b}, \eta, \theta) := f_3(\widetilde{b} + b_0, \eta, \theta); \tag{3.5}$$

$$\widetilde{f_4}(\widetilde{q}, \eta, \theta) := f_4(\widetilde{q} + q_0, \eta, \theta). \tag{3.6}$$

With the above definitions, the model becomes

$$\begin{cases} \dot{\widetilde{b}} - \Delta \widetilde{b} = \widetilde{f_1}(\widetilde{b}) & \text{in } \Omega; \\ \dot{\widetilde{q}} - d_\Omega \Delta \widetilde{q} = \widetilde{f_2}(\widetilde{q}) & \text{in } \Omega; \\ \dot{\eta} - \Delta_\Gamma \eta = \widetilde{f_3}(\widetilde{b}, \eta, \theta) & \text{on } \Gamma; \\ \dot{\theta} - d_\Gamma \Delta_\Gamma \theta = \widetilde{f_4}(\widetilde{q}, \eta, \theta) & \text{on } \Gamma, \end{cases} \tag{3.7}$$

which, this time, is conveniently endowed with completely homogeneous BCs:

$$\begin{cases} \nabla \widetilde{b} \cdot \mathbf{n} = -\widetilde{f_3}(\widetilde{b}, \eta, \theta)\psi_\eta & \text{on } \Gamma; \\ \nabla \widetilde{q} \cdot \mathbf{n} = -\widetilde{f_4}(\widetilde{q}, \eta, \theta)\psi_\theta & \text{on } \Gamma; \\ \nabla \widetilde{b} \cdot \mathbf{n} = 0 & \text{on } \Gamma_L; \\ \nabla \widetilde{q} \cdot \mathbf{n} = 0 & \text{on } \Gamma_L; \\ \widetilde{b} = 0 & \text{on } \Gamma_T; \\ \widetilde{q} = 0 & \text{on } \Gamma_T. \end{cases} \tag{3.8}$$

3.2. Step 2: weak formulation

To write a discrete formulation of the auxiliary problem (3.7)-(3.8), we define the space of trivariate spatial functions that ensure the well-posedness of the model (3.7) and fulfil the BCs (3.8):

$$H_B^1(\Omega) := \{u \in H^1(\Omega) \mid u_{|\Gamma_T} = 0 \ \wedge \ u_{|\Gamma} \in H^1(\Gamma)\}. \tag{3.9}$$

The dual space of $H_B^1(\Omega)$ will be denoted by $H_B^{-1}(\Omega)$. Following [8], the weak formulation of (3.7)-(3.8) is: find $\widetilde{b}, \widetilde{q} \in L^2([0, T]; H_B^1(\Omega))$ and $\eta, \theta \in L^2([0, T]; H^1(\Gamma))$ with $\dot{\widetilde{b}}, \dot{\widetilde{q}} \in L^2([0, T]; H_B^{-1}(\Omega))$ and

$\dot{\eta}, \dot{\theta} \in L^2([0, T]; H^{-1}(\Gamma))$ such that

$$
\begin{cases}
\int_\Omega \dot{\widetilde{b}}\varphi + \int_\Omega \nabla\widetilde{b} \cdot \nabla\varphi = \int_\Omega \widetilde{f_1}(\widetilde{b})\varphi - \psi_\eta \int_\Gamma \widetilde{f_3}(\widetilde{b}, \eta, \theta)\varphi; \\[2mm]
\int_\Omega \dot{\widetilde{q}}\varphi + d_\Omega \int_\Omega \nabla\widetilde{q} \cdot \nabla\varphi = \int_\Omega \widetilde{f_2}(\widetilde{q})\varphi - d_\Omega\psi_\theta \int_\Gamma \widetilde{f_4}(\widetilde{q}, \eta, \theta)\varphi; \\[2mm]
\int_\Gamma \dot{\eta}\phi + \int_\Gamma \nabla_\Gamma\eta \cdot \nabla_\Gamma\phi = \int_\Gamma \widetilde{f_3}(\widetilde{b}, \eta, \theta)\phi; \\[2mm]
\int_\Gamma \dot{\theta}\phi + d_\Gamma \int_\Gamma \nabla_\Gamma\theta \cdot \nabla_\Gamma\phi = \int_\Gamma \widetilde{f_4}(\widetilde{q}, \eta, \theta)\phi,
\end{cases}
\tag{3.10}
$$

for all $\varphi \in L^2([0, T]; H_B^1(\Omega))$ and $\phi \in L^2([0, T]; H^1(\Gamma))$. The weak formulation (3.10) is well-posed for sufficiently short times thanks to the following result.

Lemma 1 (Well-posedness and stability estimates for the weak formulation)**.** *There exist $c, T > 0$ depending on the parameters of the model* (2.2) *such that the solution $(\widetilde{b}, \widetilde{q}, \eta, \theta)$ of the weak problem* (3.10) *exists and is unique for $t \in [0, T]$ and fulfills the estimates*

$$
\sup_{t \in [0,T]} \|(\widetilde{b}, \widetilde{q})\|_{L^2(\Omega)} + \|(\eta, \theta)\|_{L^2(\Gamma)} + \int_0^T \left(|(\widetilde{b}, \widetilde{q})|_{H^1(\Omega)} + |(\eta, \theta)|_{H^1(\Gamma)} \right)
$$
$$
\leq c \left(1 + \|(\widetilde{b}_0, \widetilde{q}_0)\|_{L^2(\Omega)} + \|(\eta_0, \theta_0)\|_{L^2(\Gamma)} \right);
\tag{3.11}
$$

$$
\int_0^T \left(\|(\dot{\widetilde{b}}, \dot{\widetilde{q}})\|_{L^2(\Omega)} + \|(\dot{\eta}, \dot{\theta})\|_{L^2(\Gamma)} \right) + \sup_{t \in [0,T]} \left(|(\widetilde{b}, \widetilde{q})|_{H^1(\Omega)} + |(\eta, \theta)|_{H^1(\Gamma)} \right)
$$
$$
\leq c \left(1 + \|(\widetilde{b}_0, \widetilde{q}_0)\|_{H^1(\Omega)} + \|(\eta_0, \theta_0)\|_{H^1(\Gamma)} \right).
\tag{3.12}
$$

Proof. The weak problem (3.10) falls in the class of BS-RDSs considered in [8], with the difference that in the BS-DIB model considered here, the kinetics f_1, f_2, f_3, f_4 are polynomials and are therefore only locally Lipschitz, rather that globally Lipschitz as in [8]. This lemma is thus proven exactly as [8, Lemma 4.1], with the difference that the resulting estimates (3.11)-(3.12) hold only for sufficiently small final time T. $\qquad\square$

Remark 1 (Long time existence)**.** *Lemma 1 proves existence of a weak solution only for short times. When the kinetics are nonlinear as in the BS-DIB model* (2.2)*, one way to prove long time existence is proving that the model possesses an invariant region, see [18]. The existence and the size of an invariant region might depend on the parameters of the considered BS-RDS model. For the BS-DIB model* (2.2)*, a study of its invariant regions -if any- is one of our future research directions.*

3.3. *Step 3: spatially discrete formulation*

We will now describe the spatial formulation obtained by the BS-VEM following [8]. The choice of the BS-VEM to solve the model (2.2) is motivated by the possibility of using graded meshes that make the BS-VEM particularly competitive in this case by avoiding unnecessarily refinement away from the surface Γ. The choice of a convenient mesh will be illustrated in the next Section. For now, we illustrate the BS-VEM for arbitrary meshes.

Let us decompose the bulk Ω as the union of non-overlapping polyhedra, $\Omega = \cup_{E \in \mathcal{E}_h} E$. If $\mathcal{F}_f$ is the set of the faces of $\mathcal{E}_h$ that are contained in Γ, then we can write $\Gamma = \cup_{F \in \mathcal{F}_h} F$. For a face $F \in \mathcal{F}_h$, the *boundary space* $\mathbb{B}(\partial F)$ is defined by

$$\mathbb{B}(\partial F) := \{v \in C^0(\partial F) \mid v_e \in \mathbb{P}_1(e) \ \forall e \in \text{edges}(F)\}. \tag{3.13}$$

The *preliminary space* of a face F is defined by

$$\widetilde{\mathbb{V}}(F) := \{v \in H^1(F) \mid v_{|\partial F} \in \mathbb{B}(\partial F) \wedge \Delta v \in \mathbb{P}_1(F)\}. \tag{3.14}$$

The H^1 projector on faces $\Pi_F^\nabla : \widetilde{\mathbb{V}}(F) \to \mathbb{P}_1(F)$ is defined, for any $v \in \widetilde{\mathbb{V}}(F)$ by

$$\int_F \nabla(v - \Pi_F^\nabla v) \cdot \nabla p = 0 \ \forall p \in \mathbb{P}_1(F) \quad \wedge \quad \int_F (v - \Pi_F^\nabla v) = 0. \tag{3.15}$$

Then, the *enhanced VEM space* on the face F is defined by

$$\mathbb{V}(F) := \left\{ v \in \widetilde{\mathbb{V}}(F) \ \middle| \ \int_F (v - \Pi_F^\nabla v)p = 0 \ \forall p \in \mathbb{P}_1(F) \right\}. \tag{3.16}$$

For a polyhedron $E \in \mathcal{E}_h$, the *boundary space* $\mathbb{B}(\partial E)$ is defined by

$$\mathbb{B}(\partial E) := \{u \in C^0(\partial E) \mid u_{|F} \in \mathbb{V}(F) \ \forall F \in \text{faces}(E)\}. \tag{3.17}$$

At this point, the *preliminary VEM space* on E is defined by

$$\widetilde{\mathbb{V}}(E) := \{u \in H^1(E) \mid u_{|\partial E} \in \mathbb{B}(\partial E) \wedge \Delta u \in \mathbb{P}_1(E)\}. \tag{3.18}$$

The H^1 projector $\Pi_E^\nabla : \widetilde{\mathbb{V}}(E) \to \mathbb{P}_1(E)$ on the polyhedron E is defined, for each $u \in \widetilde{\mathbb{V}}(E)$, by

$$\int_E \nabla(u - \Pi_E^\nabla u) \cdot \nabla p = 0 \ \forall p \in \mathbb{P}_1(E) \quad \wedge \quad \int_E (u - \Pi_E^\nabla u) = 0. \tag{3.19}$$

Finally, the *enhanced VEM space* on the polyhedron E is defined by

$$\mathbb{V}(E) := \left\{ u \in \widetilde{\mathbb{V}}(E) \ \middle| \ \int_E (u - \Pi_E^\nabla u)p = 0 \ \forall p \in \mathbb{P}_1(E) \right\}. \tag{3.20}$$

It is well-known that the degrees of freedom in $\mathbb{V}(F)$ and $\mathbb{V}(E)$ are the pointwise values on vertexes, see [19]. The global VEM spaces are defined by matching the degrees of freedom across elements. To this end, let $\mathbb{S}_\Gamma$ and $\mathbb{S}_\Omega$ be the 1-skeleton of Γ and the 2-skeleton of Ω, respectively, defined by

$$\mathbb{S}_\Gamma := \bigcup_{F \in \mathcal{F}_h} \partial F, \qquad \mathbb{S}_\Omega := \bigcup_{E \in \mathcal{E}_h} \partial E. \tag{3.21}$$

The global VEM spaces $\mathbb{V}_\Gamma$ and $\mathbb{V}_\Omega$ are then defined as

$$\mathbb{V}_\Gamma := \{v \in H^1(\Gamma) \mid v \in C^0(\mathbb{S}_\Gamma) \ \wedge \ v_{|F} \in \mathbb{V}(F) \ \forall F \in \mathcal{F}_h\}; \tag{3.22}$$

$$\mathbb{V}_\Omega := \{u \in H^1(\Omega) \mid u \in C^0(\mathbb{S}_\Omega) \ \wedge \ u_{|E} \in \mathbb{V}(E) \ \forall E \in \mathcal{E}_h \ \wedge \ u(x, y, L) = 0 \ \forall(x, y) \in [0, L]^2\}. \tag{3.23}$$

Notice that the space $\mathbb{V}_\Omega$ reflects the homogeneous Dirichlet BCs of the continuous counterpart $H_B^1(\Omega)$. To obtain a spatially discrete counterpart of the weak formulation (3.10), we need suitable discrete bilinear forms. Following [8], for all $F \in \mathcal{F}_h$, $E \in \mathcal{E}_h$, $v, w \in \mathbb{V}(F)$ and $u, z \in \mathbb{V}(E)$, we define

$$m_F(v, w) := \int_F \Pi_F^0 v \Pi_F^0 w + h_F^2 \langle \mathrm{dof}(v - \Pi_F^0 v), \mathrm{dof}(w - \Pi_F^0 w) \rangle; \tag{3.24}$$

$$a_F(v, w) := \int_F \nabla \Pi_F^\nabla v \cdot \nabla \Pi_F^\nabla w + \langle \mathrm{dof}(v - \Pi_F^0 v), \mathrm{dof}(w - \Pi_F^0 w) \rangle; \tag{3.25}$$

$$m_E(u, z) := \int_E \Pi_E^0 u \Pi_E^0 z + h_E^3 \langle \mathrm{dof}(u - \Pi_E^0 u), \mathrm{dof}(z - \Pi_E^0 z) \rangle; \tag{3.26}$$

$$a_E(u, z) := \int_E \nabla \Pi_E^\nabla u \cdot \nabla \Pi_E^\nabla z + h_E \langle \mathrm{dof}(u - \Pi_E^0 u), \mathrm{dof}(z - \Pi_E^0 z) \rangle, \tag{3.27}$$

where h_F and h_E are the diameters of F and E, respectively. In (3.24)–(3.27), the simplest form of stabilization was chosen, the so-called *dofi-dofi* stabilization [20], for two reasons. First, this choice is the most implementation-friendly, see [21]. Second, the dofi-dofi stabilization is known to perform well when the mesh is composed of elements that are not distorted and with very regular shapes [20], which is exactly our case as we will see.

Let $m_h^\Gamma, a_h^\Gamma : \mathbb{V}_\Gamma \times \mathbb{V}_\Gamma \to \mathbb{R}$ and $m_h^\Omega, a_h^\Omega : \mathbb{V}_\Omega \times \mathbb{V}_\Omega \to \mathbb{R}$ be the corresponding global forms. Furthermore, let $I_\Gamma : C^0(\Gamma) \to \mathbb{V}_\Gamma$ and $I_\Omega : C^0(\Omega) \to \mathbb{V}_\Omega$ be the Lagrangian interpolant operators. The spatially discrete formulation is finally given by: find $B, Q : \mathbb{V}_\Omega \times [0, T]$ and $\Lambda, \Theta : \mathbb{V}_\Gamma \times [0, T] \to \mathbb{R}$ such that

$$\begin{cases} m_h^\Omega\left(\dot{B}, \Phi\right) + a_h^\Omega(B, \Phi) = m_h^\Omega\left(I_\Omega \widetilde{f_1}(B), \Phi\right) - \psi_\eta m_h^\Gamma\left(I_\Gamma \widetilde{f_3}(B, \Lambda, \Theta), \Phi\right); \\ m_h^\Omega\left(\dot{Q}, \Phi\right) + d_\Omega a_h^\Omega(Q, \Phi) = m_h^\Omega\left(I_\Omega \widetilde{f_2}(Q), \Phi\right) - d_\Omega \psi_\theta m_h^\Gamma\left(I_\Gamma \widetilde{f_4}(Q, \Lambda, \Theta), \Phi\right); \\ m_h^\Gamma\left(\dot{\Lambda}, \Psi\right) + a_h^\Gamma(\Lambda, \Psi) = m_h^\Gamma\left(I_\Gamma \widetilde{f_3}(B, \Lambda, \Theta), \Psi\right); \\ m_h^\Gamma\left(\dot{\Theta}, \Psi\right) + d_\Gamma a_h^\Gamma(\Theta, \Psi) = m_h^\Gamma\left(I_\Gamma \widetilde{f_4}(Q, \Lambda, \Theta), \Psi\right), \end{cases} \tag{3.28}$$

for all $\Phi : \mathbb{V}_\Omega \times [0, T] \to \mathbb{R}$ and $\Psi : \mathbb{V}_\Gamma \times [0, T] \to \mathbb{R}$. If $N_\Gamma := \dim \mathbb{V}_\Gamma$ and $N_\Omega := \dim \mathbb{V}_\Omega$, let $\{\psi_i\}_{i=1}^{N_\Gamma}$ and $\{\varphi_i\}_{i=1}^{N_\Omega}$ be the Lagrangian bases of $\mathbb{V}_\Gamma$ and $\mathbb{V}_\Omega$, respectively. The spatially discrete formulation (3.28) is well-posed for sufficiently short times thanks to the following result.

Lemma 2 (Well-posedness and stability estimates for the spatially discrete formulation). *There exist $c, T > 0$ depending on the parameters of the model* (2.2) *and on the shape regularity of the mesh such that the solution* (B, Q, Λ, Θ) *of the spatially discrete problem* (3.28) *exists and is unique for $t \in [0, T]$ and fulfills the estimates*

$$\sup_{t \in [0,T]} \|(B, Q)\|_{L^2(\Omega)} + \|(\Lambda, \Theta)\|_{L^2(\Gamma)} + \int_0^T \left(|(B, Q)|_{H^1(\Omega)} + |(\Lambda, \Theta)|_{H^1(\Gamma)} \right)$$
$$\leq c \left(1 + \|(B_0, Q_0)\|_{L^2(\Omega)} + \|(\Lambda_0, \Theta_0)\|_{L^2(\Gamma)} \right); \tag{3.29}$$

$$\int_0^T \left(\|(\dot{B}, \dot{Q})\|_{L^2(\Omega)} + \|(\dot{\Lambda}, \dot{\Theta})\|_{L^2(\Gamma)} \right) + \sup_{t \in [0,T]} \left(|(B, Q)|_{H^1(\Omega)} + |(\Lambda, \Theta)|_{H^1(\Gamma)} \right)$$
$$\leq c \left(1 + \|(B_0, Q_0)\|_{H^1(\Omega)} + \|(\Lambda_0, \Theta_0)\|_{H^1(\Gamma)} \right). \tag{3.30}$$

Proof. This result was proven in [8] in the case when the kinetics f_1, f_2, f_3, f_4 are globally Lipschitz. Here, f_1, f_2, f_3, f_4 are only locally Lipschitz, therefore the resulting estimates (3.29)-(3.30) hold only for sufficiently small final time T. $\qquad\square$

Remark 2 (Long time existence for the spatially discrete solution). *Lemma 2 proves existence of a spatially discrete solution only for short times. To prove long time existence, a sufficient condition would not only involve an invariant region as for the continuous problem* (2.2), *see Remark 1, but also a spatial method that preserves the invariant regions of the continuous model, see for instance [22] for the case of surface-only RDSs. To the best of our knowledge, a BS-VEM that preserves invariant regions under discretization is an open problem. It must be noted, however, that in our numerical experiments in Section 4, long time numerical solutions are found.*

We express the numerical solution (B, Q, Λ, Θ) in the Lagrange bases:

$$B(\mathbf{x}, t) = \sum_{i=1}^{N_\Omega} b_i(t)\varphi_i(\mathbf{x}), \qquad (\mathbf{x}, t) \in \Omega \times [0, T]; \tag{3.31}$$

$$Q(\mathbf{x}, t) = \sum_{i=1}^{N_\Omega} q_i(t)\varphi_i(\mathbf{x}), \qquad (\mathbf{x}, t) \in \Omega \times [0, T]; \tag{3.32}$$

$$\Lambda(\mathbf{x}, t) = \sum_{i=1}^{N_\Gamma} \lambda_i(t)\psi_i(\mathbf{x}), \qquad (\mathbf{x}, t) \in \Gamma \times [0, T]; \tag{3.33}$$

$$\Theta(\mathbf{x}, t) = \sum_{i=1}^{N_\Gamma} \theta_i(t)\psi_i(\mathbf{x}), \qquad (\mathbf{x}, t) \in \Gamma \times [0, T], \tag{3.34}$$

where $b_i(t), q_i(t), \lambda_i(t), \theta_i(t)$ are unknown time-dependent coefficients, which are collected in column vectors $\mathbf{b}(t), \mathbf{q}(t) \in \mathbb{R}^{N_\Omega}$, $\boldsymbol{\eta}(t), \boldsymbol{\theta}(t) \in \mathbb{R}^{N_\Gamma}$. Following [8], we substitute (3.31)–(3.34) into the spatially discrete formulation (3.28), and we obtain the following ODE system in vector form:

$$\begin{cases} M_\Omega \dot{\mathbf{b}} + A_\Omega \mathbf{b} = M_\Omega \widetilde{f_1}(\mathbf{b}) - \psi_\eta R M_\Gamma \widetilde{f_3}(\mathbf{b}, \boldsymbol{\eta}, \boldsymbol{\theta}); \\ M_\Omega \dot{\mathbf{q}} + d_\Omega A_\Omega \mathbf{q} = M_\Omega \widetilde{f_2}(\mathbf{q}) - d_\Omega \psi_\theta R M_\Gamma \widetilde{f_4}(\mathbf{q}, \boldsymbol{\eta}, \boldsymbol{\theta}); \\ M_\Gamma \dot{\boldsymbol{\eta}} + A_\Gamma \boldsymbol{\eta} = M_\Gamma \widetilde{f_3}(\mathbf{b}, \boldsymbol{\eta}, \boldsymbol{\theta}); \\ M_\Gamma \dot{\boldsymbol{\theta}} + d_\Gamma A_\Gamma \boldsymbol{\theta} = M_\Gamma \widetilde{f_4}(\mathbf{q}, \boldsymbol{\eta}, \boldsymbol{\theta}), \end{cases} \tag{3.35}$$

where the stiffness matrices $A_\Omega \in \mathbb{R}^{N_\Omega \times N_\Omega}$, $A_\Gamma \in \mathbb{R}^{N_\Gamma \times N_\Gamma}$, the lumped mass matrices $M_\Omega \in \mathbb{R}^{N_\Omega \times N_\Omega}$, $M_\Gamma \in \mathbb{R}^{N_\Gamma \times N_\Gamma}$ and the reduction matrix $R \in \mathbb{R}^{N_\Omega \times N_\Gamma}$ are defined as follows:

$$(A_\Omega)_{ij} := a_h^\Omega(\varphi_i, \varphi_j), \qquad (M_\Omega)_{ij} := m_h^\Omega(\varphi_i, \varphi_j), \qquad i, j = 1, \ldots, N_\Omega; \tag{3.36}$$

$$(A_\Gamma)_{ij} := a_h^\Gamma(\psi_i, \psi_j), \qquad (M_\Gamma)_{ij} := m_h^\Gamma(\psi_i, \psi_j), \qquad i, j = 1, \ldots, N_\Gamma; \tag{3.37}$$

$$R = \begin{bmatrix} I_{N_\Gamma} \\ 0 \end{bmatrix}, \tag{3.38}$$

where I_{N_Γ} is the identity of dimension N_Γ.

3.4. Step 4: fully discrete formulation in vector form

Following [8], we discretize in time the ODE system (3.35) with the IMEX Euler scheme, which is first-order accurate. Let $\tau > 0$ be the time stepsize and let $N_T = \left\lceil \frac{T}{\tau} \right\rceil$ be the number of timesteps. For all $n = 0, \ldots, N_T - 1$, the fully discrete solution $(\mathbf{b}^{(n)}, \mathbf{q}^{(n)}, \boldsymbol{\eta}^{(n)}, \boldsymbol{\theta}^{(n)})$ at time $t_n := n\tau$ is found as follows:

$$\begin{cases} (M_\Omega + \tau A_\Omega)\mathbf{b}^{(n+1)} = M_\Omega \mathbf{b}^{(n)} + \tau \left(M_\Omega \mathbf{f}_1^{(n)} - \psi_\eta R M_\Gamma \mathbf{f}_3^{(n)} \right); \\ (M_\Omega + d_\Omega \tau A_\Omega)\mathbf{q}^{(n+1)} = M_\Omega \mathbf{q}^{(n)} + \tau \left(M_\Omega \mathbf{f}_2^{(n)} - \psi_\theta d_\Omega R M_\Gamma \mathbf{f}_4^{(n)} \right); \\ (M_\Gamma + \tau A_\Gamma)\boldsymbol{\eta}^{(n+1)} = M_\Gamma \boldsymbol{\eta}^{(n)} + \tau M_\Gamma \mathbf{f}_3^{(n)}; \\ (M_\Gamma + d_\Gamma \tau A_\Gamma)\boldsymbol{\theta}^{(n+1)} = M_\Gamma \boldsymbol{\theta}^{(n)} + \tau M_\Gamma \mathbf{f}_4^{(n)}, \end{cases} \tag{3.39}$$

where

$$\mathbf{f}_1^{(n)} := \widetilde{f_1}(\mathbf{b}^{(n)}); \quad \mathbf{f}_2^{(n)} := \widetilde{f_2}(\mathbf{q}^{(n)}); \quad \mathbf{f}_3^{(n)} := \widetilde{f_3}(\mathbf{b}^{(n)}, \boldsymbol{\eta}^{(n)}, \boldsymbol{\theta}^{(n)}); \quad \mathbf{f}_4^{(n)} := \widetilde{f_4}(\mathbf{q}^{(n)}, \boldsymbol{\eta}^{(n)}, \boldsymbol{\theta}^{(n)}).$$

The fully discrete formulation (3.39) is composed of four linear algebraic systems that can be solved independently of each other at each time step. Of these four linear systems, two have dimension N_Ω, while the other two have dimension N_Γ. If the cube Ω is discretised with a Cartesian mesh with $N_x \in \mathbb{N}$ gridpoints along each dimension, then $N_\Omega = N_x^2(N_x - 1)$ due to the boundary conditions, which makes the linear systems in (3.39) computationally expensive to solve. An extremely efficient approach to address this issue is the so-called Matrix-Oriented Finite Element Method (MO-FEM) [12, 13], which exploits the Cartesian structure of the grid to translate the linear systems in (3.39) into tensor equations of much lower size. We will show a numerical solution to our problem carried out with MO-FEM in Section 4. However, we will show that, given the particular nature of the considered PDE problem, an even more efficient solver is given by the BS-VEM on a bespoke mesh.

3.5. Bespoke BS-VEM mesh for the BS-DIB model

Since the domain of the model problem (2.2) is a cube, then it would be natural to choose an efficient numerical method that exploits the structure of Cartesian grids, such as the Matrix-Oriented Finite Element Method (MO-FEM) [12, 13]. This gives us the opportunity to show the competitiveness of BS-VEM in solving the BS-DIB model (2.2) and thus further motivates the choice of a cube as spatial domain. For this reason, we choose the cubic spatial domain $\Omega = [0, L]^3$ with $L = 50$. We choose the model parameters, the final time and and the timestep as follows: $B = 66$, $C = 3$, $A_2 = 1$, $\gamma = 0.2$, $\psi_\eta = \psi_\theta = 0.2$, $T = 50$ and $\tau = $ 2e-3. The other parameter values are as in (2.11). To demonstrate that the numerical solution tends to a stationary Turing pattern, as for instance in [2] we show, as an indicator, that the increment $\|\eta(t_{n+1}) - \eta(t_n)\|_{L^2(\Omega)}$ of the η component of the numerical solution tends to zero.

In this section, we consider a Cartesian grid with $N_x = 129$, i.e., of $129 \times 129 \times 129 \approx$ 2.15e+6 equally spaced nodes (corresponding to $128 \times 128 \times 128$ equally spaced intervals), and we show that MO-FEM produces the numerical solution shown in Figure 2. In keeping with the physical meaning of the parameter choice, we can observe that the bulk components (b, q) exhibit spatial patterns only in the proximity of the surface Γ, and become approximately constant away from Γ. This suggests that a uniform Cartesian cubic grid would be unnecessarily fine away from Γ. For this reason, we apply

the BS-VEM with a graded cubic mesh that is highly refined close to Γ and gradually becomes coarser as the distance from Γ increases. Such graded polyhedral mesh is depicted in Figure 3(a). This grid is composed of two layers of 128×128 cubic elements close to Γ, and five layers of gradually larger "false cubes", where the size of such false cubes doubles at each layer. For this reason, in the first two layers (closest to Γ) the number of cubes along each dimension is 128, a power of 2. One of the aforementioned false cubes is depicted Figure 3(b) and is actually an *ennahedron*: a polyhedron with nine faces and thirteen vertices. Specifically, such ennahedron is a cube the bottom face of which is split into four smaller square faces as shown in Figure 3(b). The proposed graded mesh provides a discretisation for the surface Γ as refined as the Cartesian grid used for the MO-FEM (129×129 nodes on Γ) and, at the same time has much less nodes (approximately $5.56e+4$ versus $2.15e+6$), resulting in a discrete problem of much smaller size and shorter computational times (approximately 89 minutes for MO-FEM and 39 minutes for BS-VEM) when the linear systems are solved with Matlab's built-in direct solver \ (backslash). It must be noted that, if we applied BS-VEM on the same Cartesian mesh used for MO-FEM, the latter method would be much quicker as it is specifically designed to exploit the tensor structure of Cartesian grids. Specifically, BS-VEM would require prohibitively large computational times and memory, at least for our limited machine. On the other hand, MO-FEM (nor classical FEM) cannot be applied on graded or adaptive meshes with hanging nodes. All in all, the reduced number of degrees of freedom of the BS-VEM mesh outweights the efficiency of MO-FEM on Cartesian grids, resulting in shorter computational times. On domains of more general shapes, where tensorized methods like MO-FEM are not generally applicable, BS-VEM on a graded mesh would be even more competitive.

(a) Bulk component b and surface component η at the final time $T = 50$.

(b) Increment of surface component η over time.
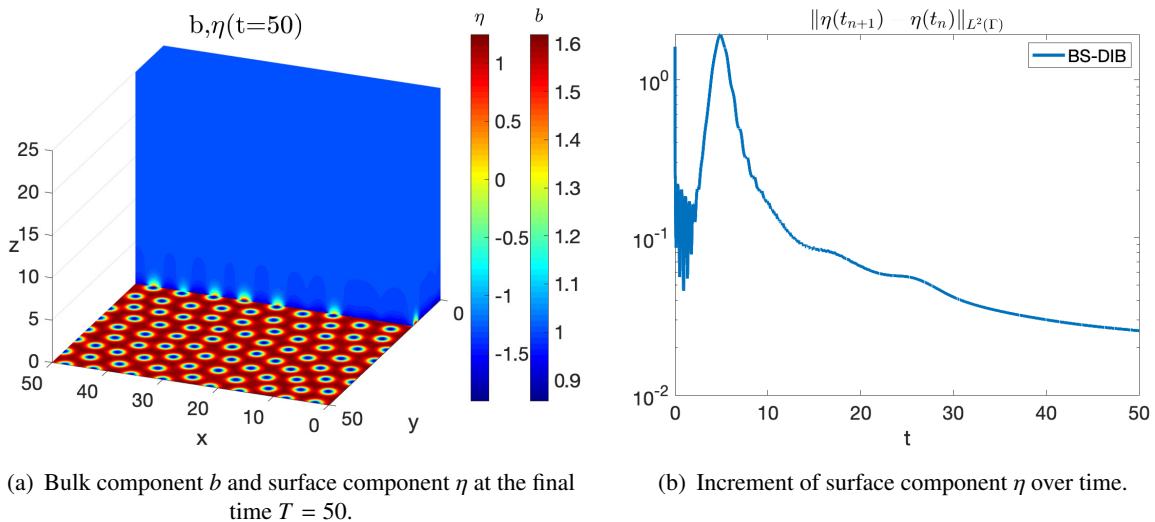
Figure 2. 3D BS-DIB model (2.2), $B = 66, C = 3, \psi_\eta = \psi_\theta = 0.2$, final time $T = 50$: simulation obtained with the MO-FEM approach described in Section 3.5. The BS-DIB model (2.2) shows a reversed spots pattern, the bulk component b exhibits a spatial pattern only in a neighborhood of the surface Γ. A similar result arises for the variables θ on the surface and q in the bulk, respectively. This suggests the usage of a graded mesh that is highly refined close to Γ and much coarser away from Γ, which we will apply in the next simulations (see Figure 3 and Section 4).

(a) Nodes of the graded mesh.　　　　　　(b) Cubic element with hanging nodes.
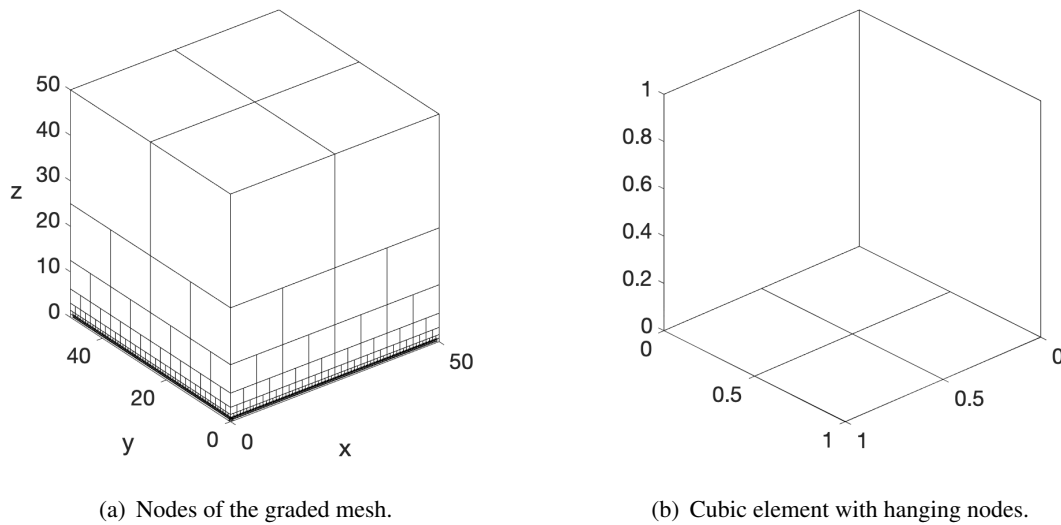
Figure 3. Graded polyhedral mesh used in the BS-VEM approximation of the model (2.2).

By comparing Figure 2 and Simulation D3 in Section 4 we observe that, for the BS-DIB model (2.2), MO-FEM and BS-VEM produce patterns of the same morphological class, i.e., reversed spots. The positioning of the patterns, however, is different, and that is to be expected because RDSs are highly sensitive to initial conditions. This implies that a small perturbation resulting from applying a different numerical method on equal initial conditions (as in (2.25)) is enough to significantly affect the positioning of the asymptotic spatial patterns, but not their morphological class [23]. Having ascertained the competitiveness of BS-VEM in solving the BS-DIB model, all the numerical experiments in Section 4 will be carried out using BS-VEM.

4. Numerical experiments

We shall present eight numerical experiments to compare the DIB model (2.1) with the novel BS-DIB model (2.2). The eight experiments differ from each other for appropriate choices of the model parameters. The first four experiments, called T1 through T4, suggest that the BS-DIB model (2.2) has a larger Turing space than the DIB model (2.1), meaning that on equal parameters, the BS-DIB model might exhibit Turing patterns while the DIB model does not. The latter four experiments, called D1 through D4, explore the effect of BS coupling on the *morphological class* of Turing patterns, meaning that on equal parameters, the DIB (2.1) and BS-DIB (2.2) models can exhibit Turing patterns of different morphological classes. All the experiments are carried out on a cubic domain of edge length $L = 50$ on the polyhedral mesh described in Section 3.5. The final time T and the timestep τ also differ for each experiment according to the stiffness of the problem and the timescale of the dynamics. A recap of the numerical experiments and the respective parameters is given in Table 1. As discussed in Section 3.5, we recall that the BS-VEM on a suitable graded mesh is more computationally efficient than MO-FEM in solving the BS-DIB model (2.2). For this reason, all the experiments presented in this Section will be carried out with BS-VEM. It must be noted that the dynamics of both the DIB (2.1) and

BS-DIB (2.2) models are affected by the parameters, therefore the convergence towards the asymptotic steady state can be more or less quick depending on the model parameters. For this reason, also in the next experiments, we present a plot of the increment $\|\eta(t_{n+1}) - \eta(t_n)\|_{L^2(\Gamma)}$ over time. We assume that if the increment at the chosen final time T is substantially lower than the peak increment corresponding to the end of the reactivity transient regime [24], then the final time solution is a good approximation of the asymptotic steady state [25].

Table 1. Recap of the numerical experiments in Section 4.

Experiment	A_2	B	C	γ	$\psi_\eta = \psi_\theta$	T	τ	Pattern BS-DIB	Pattern DIB
T1	1	50	10	0	0.5	200	2e-3	Thin worms	Homogeneous (2.24)
T2	1	75	5	0	0.3	200	2e-3	Stripes	Homogeneous (2.24)
T3	1	35	15	0	0.5	100	5e-3	Reversed spots	Homogeneous (2.24)
T4	1	30	20	0	0.5	50	5e-3	Homogeneous ($\neq \boldsymbol{\xi}^*$ in (2.24))	Homogeneous (2.24)
D1	1	66	3	0.2	0.1	200	5e-3	Reversed spots & worms	Labyrinth
D2	1	66	3	0.2	0.15	50	2e-3	Reversed spots & small worms	Labyrinth
D3	1	66	3	0.2	0.2	50	2e-3	Reversed spots	Labyrinth
D4	1	30	3	0.2	0.1	200	5e-3	Reversed spots (smaller than in DIB)	Reversed spots

4.1. Experiments T1–T4: exploration of the Turing space

In this Section, we compare the DIB (2.1) and BS-DIB (2.2) models in four experiments, called T1 through T4, where the model parameters (C, B) are chosen *outside* -but close to- the Turing space of the DIB model (2.1), i.e., the region in the parameter space (C, B) where the DIB model undergoes Turing instability and exhibits patterns, see [15]. Therefore, the DIB model does not produce patterns in these experiments as expected, and the numerical solutions early attain the stable equilibrium $\eta^* = 0, \theta^* = \alpha$ in (2.24) of which the initial condition (2.25) is a small perturbation. On the other hand, the BS-DIB model (2.2) exhibits spatial patterns in all experiments T1–T4. This suggests that the BS-DIB model has a larger Turing space than the DIB model. As mentioned before, a theoretical analysis of the Turing instability for the BS-DIB model is outside the scope of this work and is one of our current research directions. In particular, the numerical solutions η and θ on the surface Γ of the BS-DIB model have the following behaviors:

T1. Slow convergence to a thin worm pattern, where the worms slowly merge into longer worms over time, see Figure 4;

T2. Slow convergence to a stripe pattern. The transient solution exhibits spots that slowly merge into stripes over time, see Figure 5;

T3. Convergence to a reversed spots (holes) pattern, see Figure 6;

T4. Quick convergence to a homogeneous steady state different from (2.24), see Figure 7.
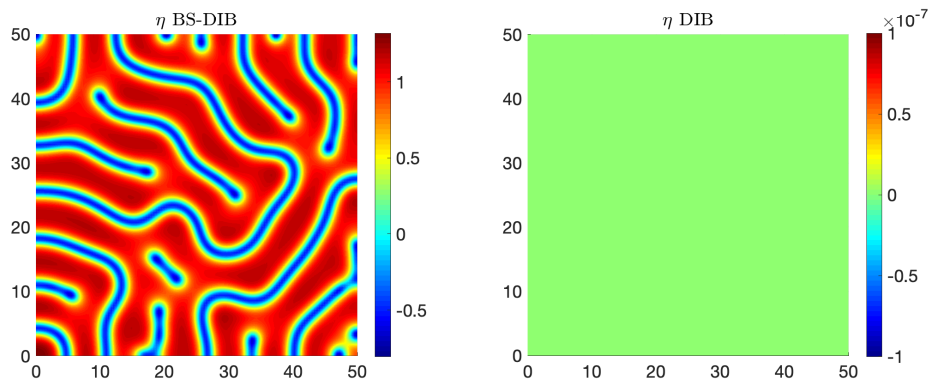
(a) Surface component η at the final time $T = 200$.
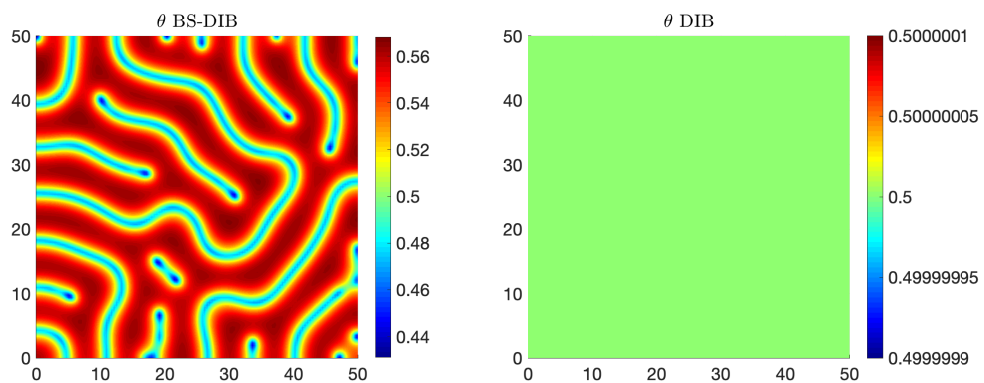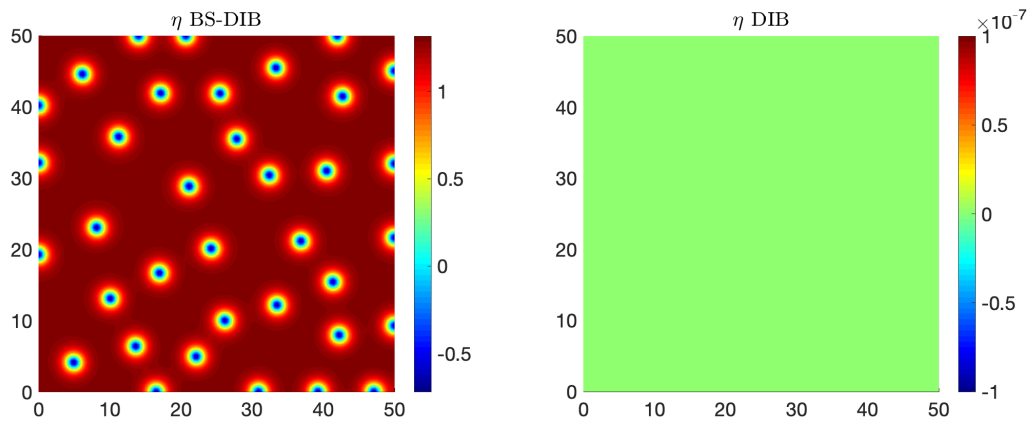

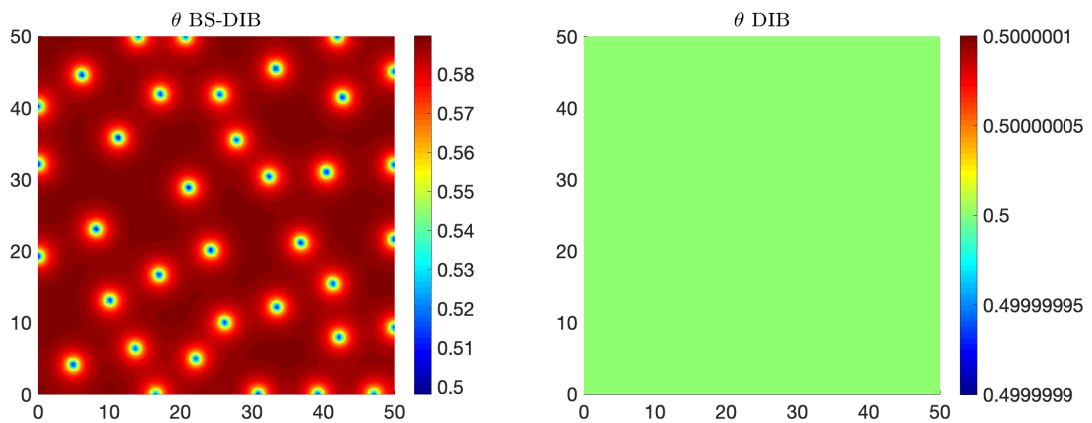(b) Surface component θ at the final time $T = 200$.
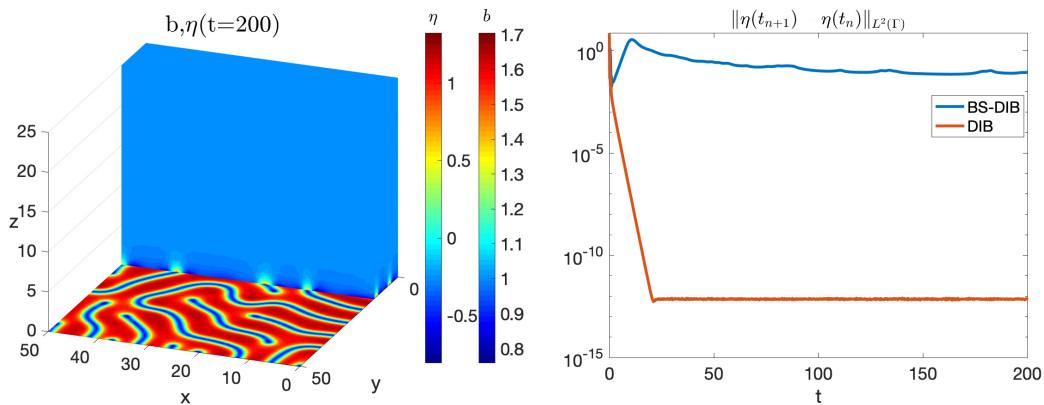
(c) bulk component b and surface component η at final time.
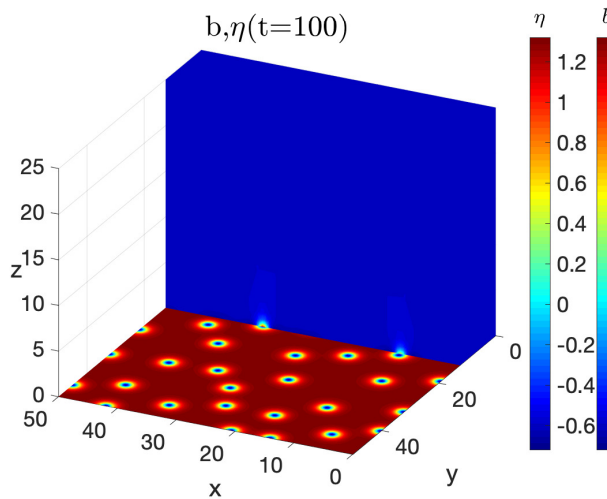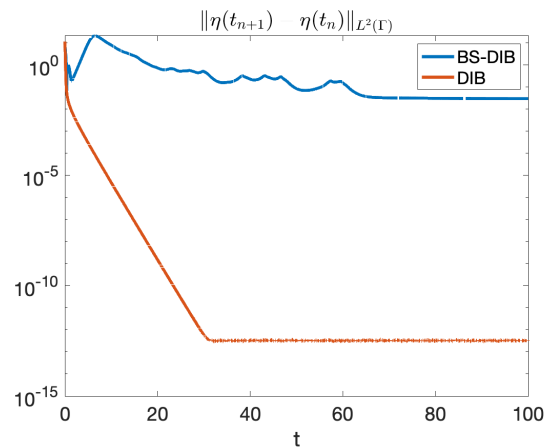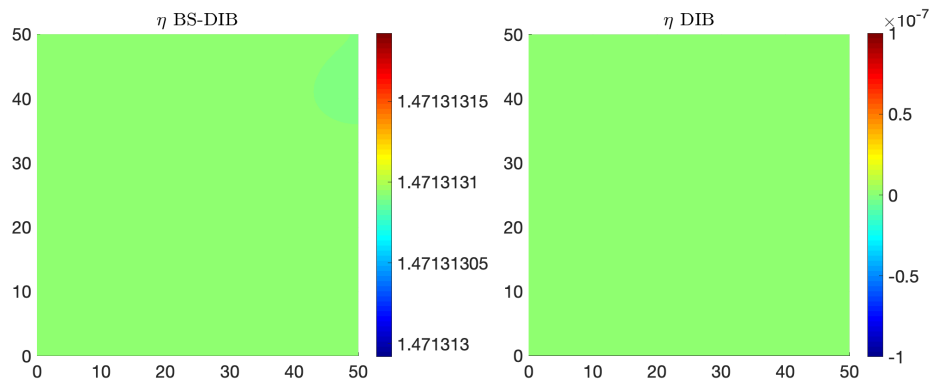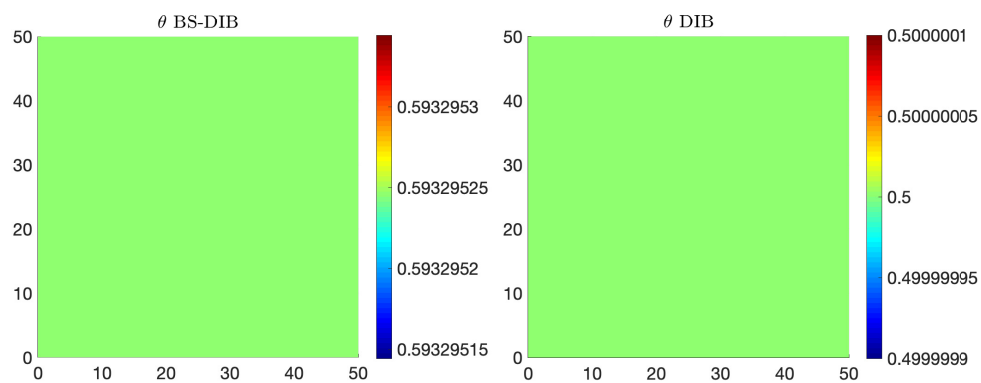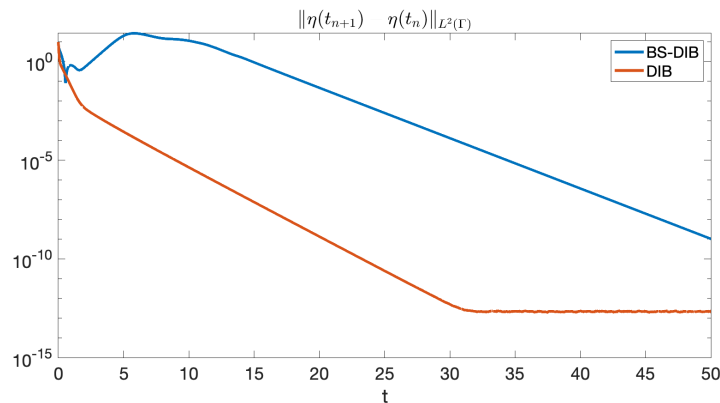
(d) Increment of surface component η over time.

Figure 4. Simulation T1. BS-DIB model (2.2), $C = 10, B = 50, \psi_\eta = \psi_\theta = 0.5$, see also Table 1. The 3D-BS-DIB solution shows a slow-to-stabilize worm pattern for η and θ on the surface Γ, while the 2D-DIB model (2.1) reaches the homogeneous steady state $(\eta^*, \theta^*) = (0, 0.5)$. In fact, in panel (d) the 3D model (blue line) appears to converge very slowly towards an asymptotic steady state. In panel (c), the z-axis is not in scale to help visualization.
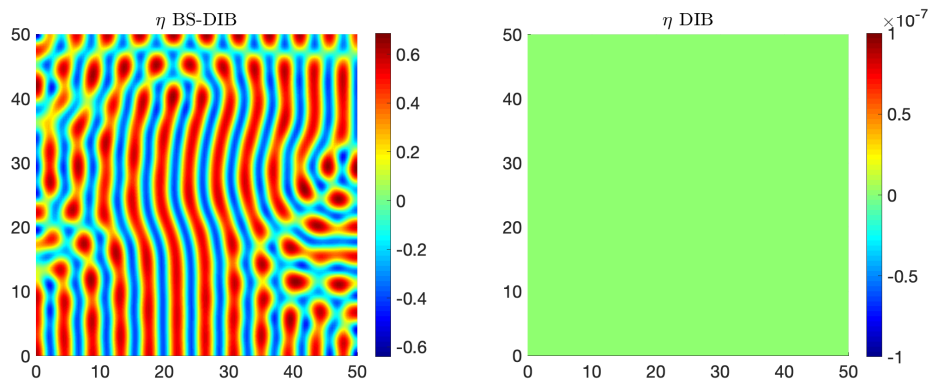
(a) Surface component η at the final time $T = 200$.
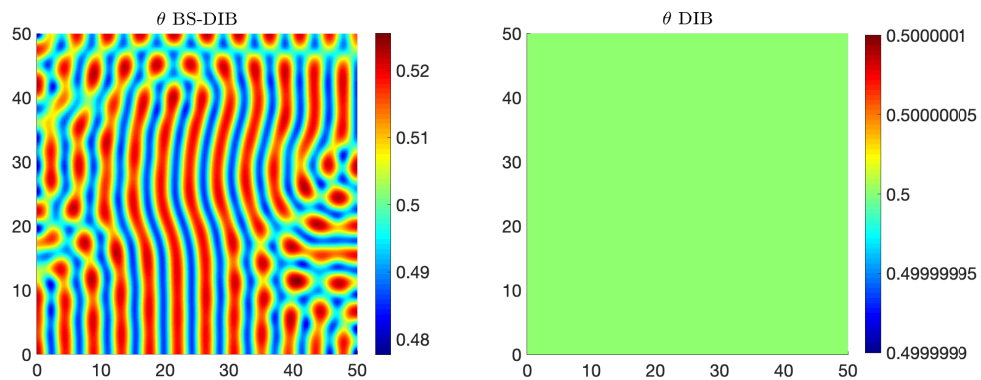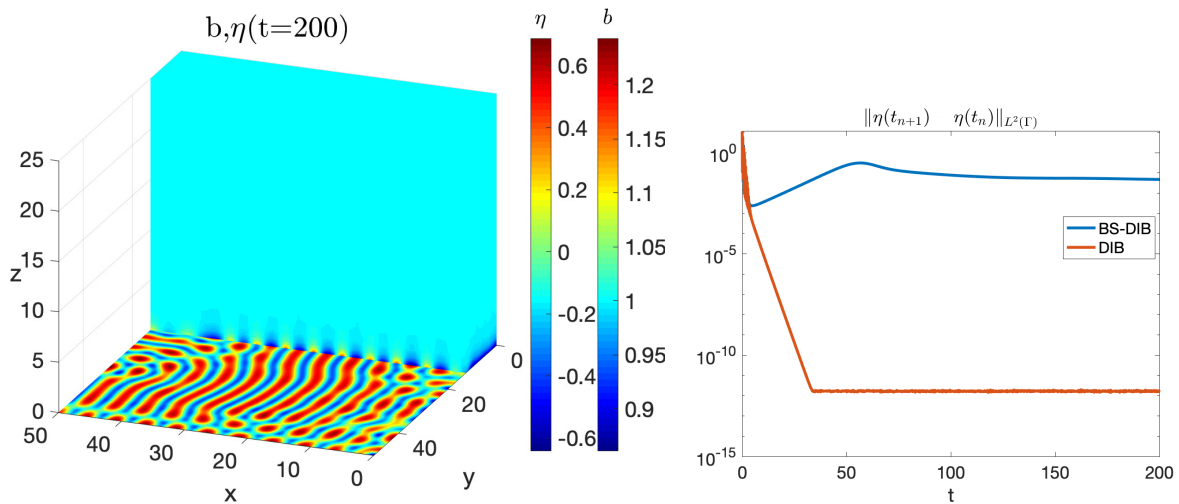
(b) Surface component θ at the final time $T = 200$.

(c) Bulk component b and surface component η at the final time.

(d) Increment of surface component η over time.

Figure 5. Simulation T2. BS-DIB model (2.2), $C = 5, B = 75, \psi_\eta = \psi_\theta = 0.3$, see also Table 1. The 3D-BS-DIB solution at $T = 200$ shows a slow-to-stabilize stripe pattern for η and θ on the surface Γ, while in the 2D-DIB model (2.1) the solution reaches the homogeneous steady state $(\eta^*, \theta^*) = (0, 0.5)$.

(a) Surface component η at the final time $T = 200$.

(b) Surface component θ at the final time $T = 200$.

(c) Bulk component b and surface component η at the final time.

(d) Increment of surface component η over time.

Figure 6. Simulation T3. BS-DIB model (2.2), $C = 15, B = 35, \psi_\eta = \psi_\theta = 0.5$, see also Table 1. The 3D BS-DIB components η and θ at $T = 100$ attain a reversed spots pattern, while in the 2D DIB model (2.1) they reach the homogeneous equilibrium $(\eta^*, \theta^*) = (0, 0.5)$.

(a) Surface component η at the final time $T = 50$.

(b) Surface component θ at the final time $T = 50$.

(c) Increment of surface component η over time.

Figure 7. Simulation T4. BS-DIB model (2.2), $C = 20, B = 30, \psi_\eta = \psi_\theta = 0.5$, see also Table 1. In the 2D-DIB model η and θ come back to the homogeneous equilibrium $(\eta^*, \theta^*) = (0, 0.5)$ of which the initial condition (2.25) is a small perturbation, while the 3D BS-DIB solution departs from ξ^* in (2.24) and reaches a different homogeneous steady state, say $(\eta^{**}, \theta^{**}) \approx (1.4713, 0.5933)$. This behaviour of the 3D model is also evident looking at the increment in panel (c) for short times.

4.2. Experiments D1–D4: effect of bulk-surface coupling on pattern formation

In this Section, we compare the DIB model (2.2) and the BS-DIB model (2.2) in four more experiments, called D1 through D4, that are devised to study the effect of coupling in the 3D model, measured by increasing the coefficients $\psi_\eta = \psi_\theta$ in (2.3). As opposed to Experiments T1–T4 in the previous Section, the parameters here are chosen *inside* the Turing space of the 2D-DIB model (2.1), in particular those for the reference labyrinth and reversed spots Turing patterns studied in [15]. The proposed simulations explore the effect of bulk-surface coupling on the morphological class of Turing patterns in the BS-DIB model, as follows.

In particular, we will show that the labyrinth breaks into more fragmented structures such as worms and holes/reversed spots: the stronger the coupling, i.e., the higher $\psi_\eta = \psi_\theta$, the more fragmented the pattern, up to the limit case when the BS-DIB pattern is composed by holes/reversed spots in Experiment D3. Moreover, Experiments D1–D3 indicate that the range and size of the bulk patterns increases with $\psi_\eta = \psi_\theta$ as illustrated below. Experiment D4 instead will show that when the 2D DIB model (2.1) exhibits holes/reversed spots, the effect of coupling is only a reduction in size of the holes.

To sum up, the outcome of Experiments D1 through D4 is as follows:

D1. For $B = 66, C = 3$ as in [15], $\psi_\eta = \psi_\theta = 0.1$, the DIB model (2.1) at $T = 200$ attains a labyrinth, while the 3D BS-DIB model (2.2) converges to a reversed spots & worms pattern, see Figure 8, as it is also evident by the behaviour of the η-increment in Figure 8;

D2. Same (B, C) as in Experiment D1, $\psi_\eta = \psi_\theta = 0.15$, the 3D BS-DIB model (2.2) attains at $T = 50$ the same morphological structure, but with shorter worms than in Experiment D1, see Figure 9;

D3. Same (B, C) as in Experiment D1, $\psi_\eta = \psi_\theta = 0.2$, the 3D BS-DIB model (2.2) converges to a holes/reversed spots pattern, see Figure 10;

D4. For $B = 30, C = 3$ as in [15], $\psi_\eta = \psi_\theta = 0.1$, at $T = 200$ both the 2D-DIB (2.1) and the 3D- BS-DIB (2.2) models converge to a holes/reversed spots pattern, where the holes are larger for the original DIB model, see Figure 11.

These results and more numerical details are reported in Table 1.

Moreover, for the Experiments D1–D3, we compare a (x, z) section of the bulk component $b(x, y, z, T)$ at the final time of integration for $y = 12.5$. In Figure 12, we show that by increasing the coupling parameters $\psi_\eta = \psi_\theta$ (left to right), the amplitude of the bulk-pattern increases (as indicated by the colorbars) and length along the z-direction, that is the morphology structures venture more significantly into the electrolyte.
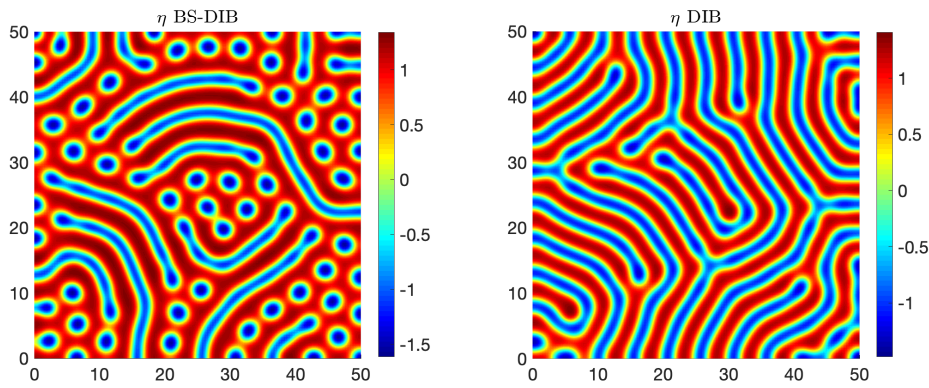
(a) Surface component η at the final time $T = 200$.
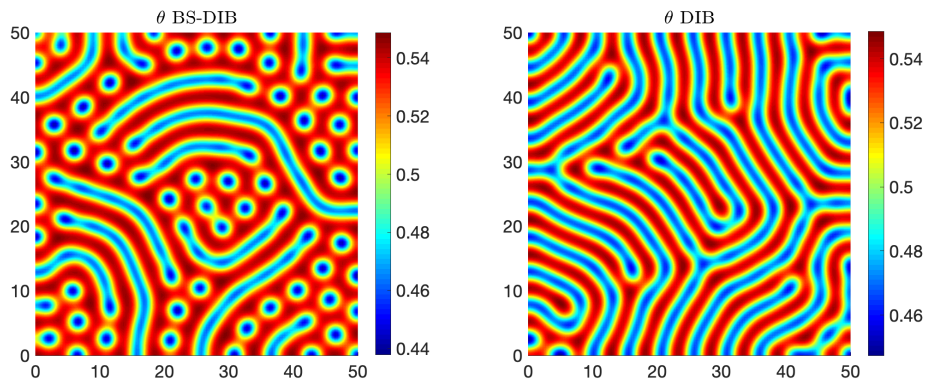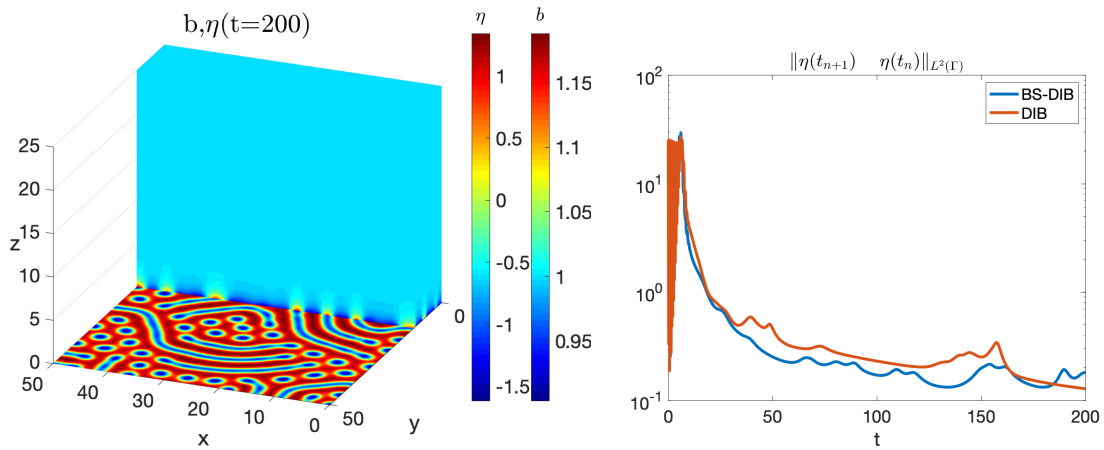
(b) Surface component θ at the final time $T = 200$.

(c) Bulk component b and surface component η.

(d) Increment of surface component η over time.

Figure 8. Simulation D1. BS-DIB model (2.2) $B = 66, C = 3, \psi_\eta = \psi_\theta = 0.1$, see also Table 1. Spot-and-worm patterns for the η and θ components of the 3D-BS-DIB model (2.2) are attained at $T = 200$, while a labyrinth is attained for the 2D DIB model (2.1) on the same interval. The spots of the spot-and-worm pattern in the coupled model (2.2) tend to slowly merge into worms over time.
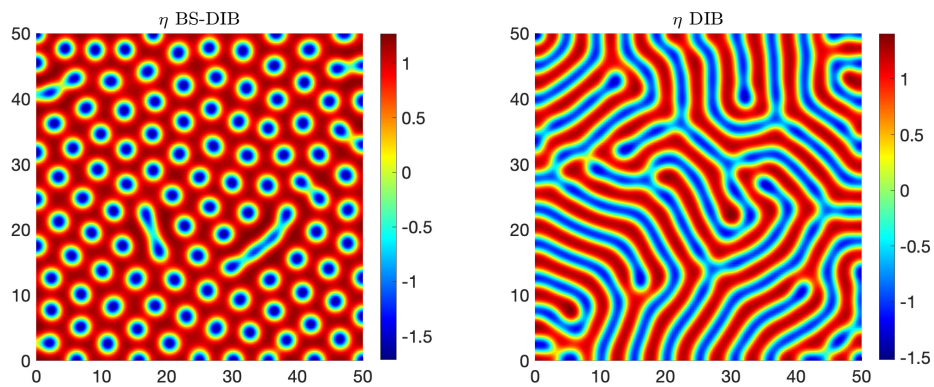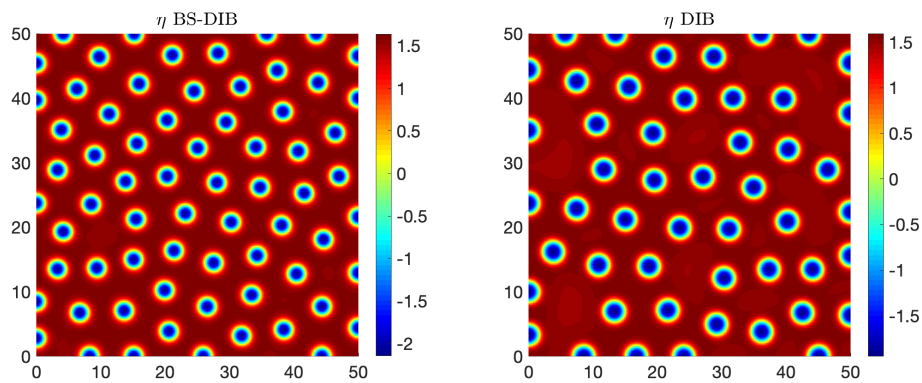
(a) Surface component η at the final time $T = 50$.
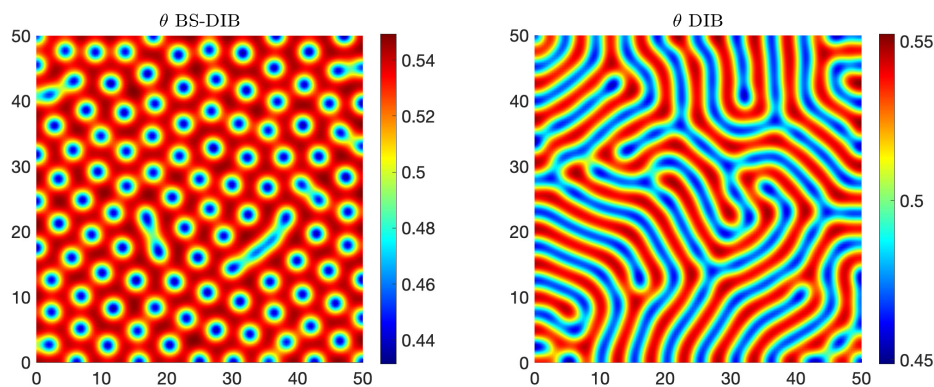
(b) Surface component θ at the final time $T = 50$.
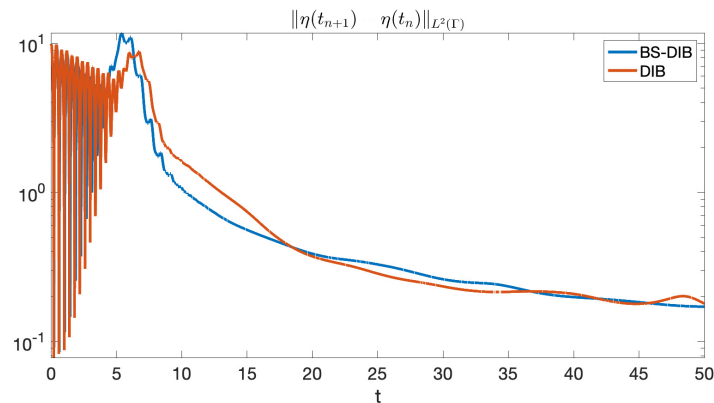
(c) Increment of surface component η over time.

Figure 9. Simulation D2. $B = 66, C = 3, \psi_\eta = \psi_\theta = 0.15$, see also Table 1. With a larger BS coupling amount, the BS-DIB model (2.2) at $T = 50$ attains a spot & worm pattern, with worms of smaller length compared to Simulation D1. For these (B, C) parameters, at $T = 50$ the 2D DIB model (2.1) still exhibits a labyrinth pattern.
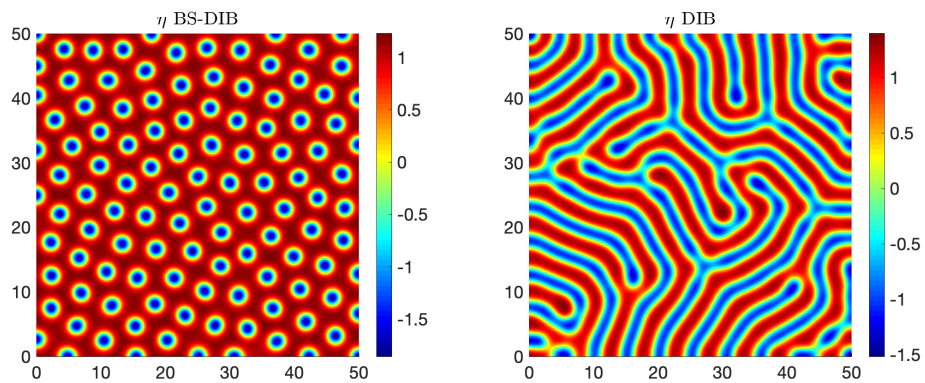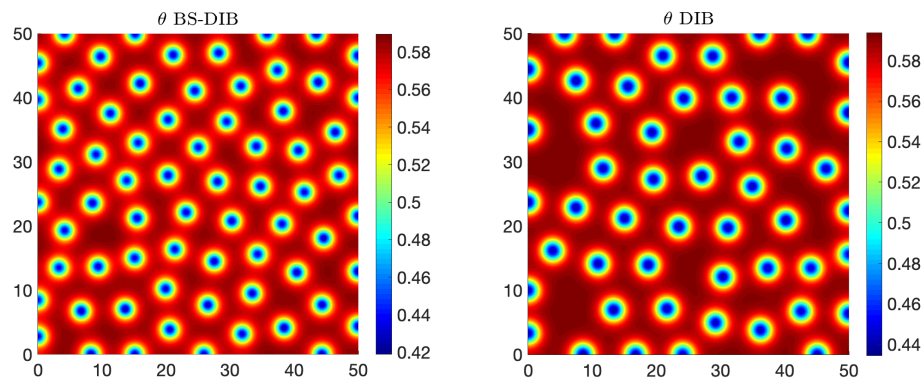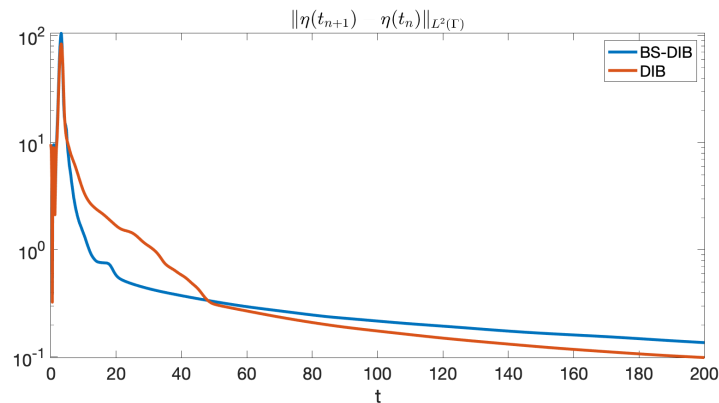
(a) Surface component η at the final time $T = 50$.
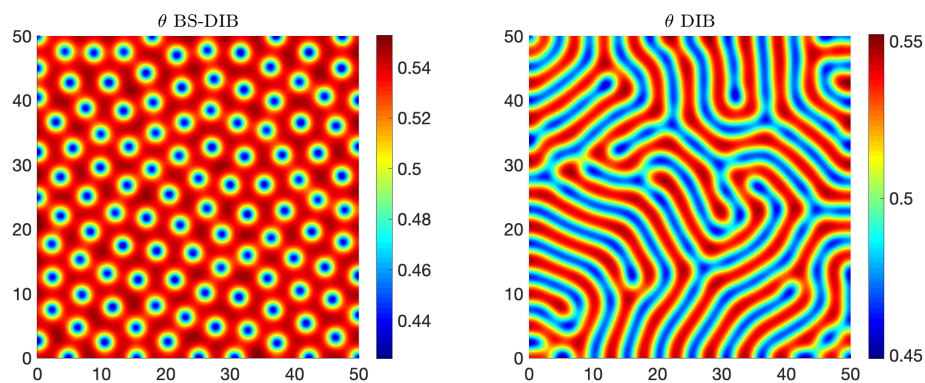
(b) Surface component θ at the final time $T = 50$.
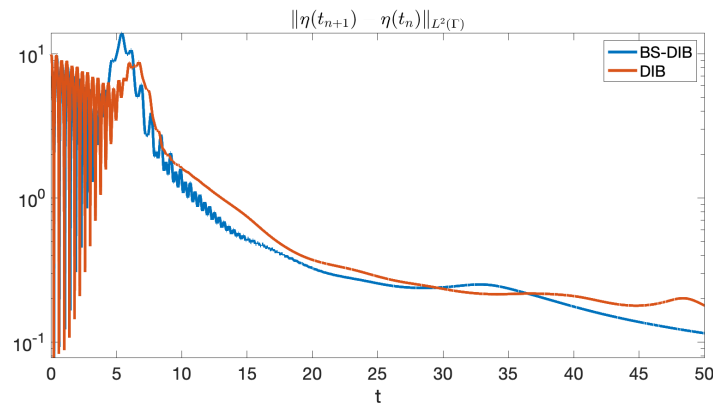
(c) Increment of surface component η over time.

Figure 10. Simulation D3. $B = 66, C = 3, \psi_\eta = \psi_\theta = 0.2$, see Table 1. By further increasing the BS coupling amount, at $T = 50$ both surface components η and θ of the 3D BS-DIB model (2.2) exhibit a reversed spots pattern, compared with the labyrinths for the uncoupled 2D DIB model (2.1). These results found by the BS-VEM method are in good agreement with those obtained with the MO-FEM approach in Figure 2, since both methods produce spatial patterns of the same morphological class.

(a) Surface component η at the final time $T = 200$.

(b) Surface component θ at the final time $T = 200$.

(c) Increment of surface component η over time.

Figure 11. Simulation D4. $B = 30, C = 3, \psi_\eta = \psi_\theta = 0.1$, see Table 1. For these parameters, at the final time $T = 200$ the η and θ components attain reversed spots patterns in both DIB and BS-DIB models. However, the coupled BS-DIB model (2.2) shows reversed spots of smaller size with higher spatial density than the 2D DIB model (2.1).
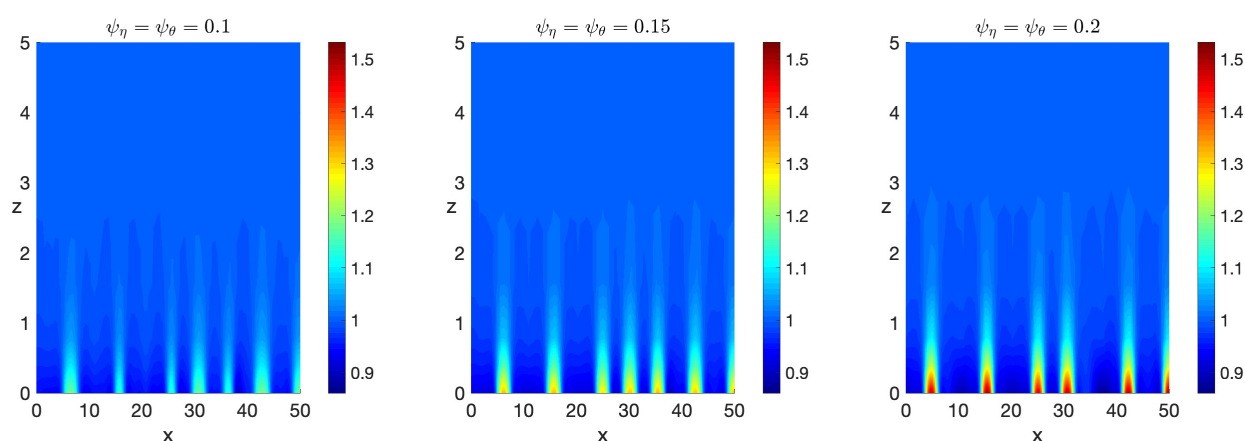
Figure 12. Comparison of a section of the bulk component *b* of Experiments D1–D3 (see Table 1) for *y* = 12.5. By increasing the coupling parameters $\psi_\eta = \psi_\theta$ (left to right), the bulk patterns increase in range (as indicated by the colorbars) and length along the *z*-direction.

5. Conclusions

We have introduced a BS-RD model in 3D, which we have called BS-DIB model, for electrodeposition and battery modeling. Compared to the previous DIB model in 2D, the new model fully accounts for the non-uniform electrolyte concentration in a neighborhood of the electrodic surface. The two-way coupling between bulk and surface substantially influences the long-term behavior of the system and in particular the morphological class of the Turing patterns obtained as asymptotic steady state solutions. Specifically, we find that the bulk-surface coupling has two main effects. First, we observe empirically that the BS-DIB model possesses a large Turing region in the parameter space, compared to the 2D DIB model. Second, when the parameters are chosen in the Turing space of the DIB model, the BS-DIB model still exhibits spatial patterns, but of a different spatial structure, i.e., the bulk-surface coupling affects the morphological class of the attained patterns. A theoretical Turing instability analysis of the BS-DIB model is beyond the scope of this work. These aspects form part of our current investigations.

The BS-DIB model is posed on a cubic domain, so it lends itself to efficient numerical solvers specifically devised for Cartesian grids, such as the MO-FEM [12]. Moreover, since the BS-DIB model exhibits spatial patterns only in a neighborhood of the surface, we have adopted the BS-VEM on a graded mesh that is highly refined close to the surface and much coarser away from the surface. Such a graded mesh combines the advantages of (i) being composed by equal elements of cubic shape, which significantly speeds up matrix assembly and improves matrix structure and (ii) has far less degrees of freedom than a uniform Cartesian grid with the same level of refinement close to the surface. For this reason, the BS-VEM on a graded mesh proves to be more computationally efficient than the MO-FEM (see discussion in Section 3.5) and is thus the spatial method of choice throughout this work. Moreover, as opposed to the MO-FEM, which is confined to structured geometries such as Cartesian grids, the BS-VEM can handle domains of general shape, thereby facilitating the simulation of real case studies.

Use of AI tools declaration

The authors declare they have not used Artificial Intelligence (AI) tools in the creation of this article.

Acknowledgments

Conflict of interest

The authors declare no conflicts of interest.

References

1. B. Bozzini, D. Lacitignola, I. Sgura, Spatio-temporal organization in alloy electrode-position: a morphochemical mathematical model and its experimental validation, *J. Solid State Electrochem.*, **17** (2013), 467–469. https://doi.org/10.1007/s10008-012-1945-7

2. D. Lacitignola, B. Bozzini, I. Sgura, Spatio-temporal organization in a morphochemical electrodeposition model: Hopf and Turing instabilities and their interplay, *Eur. J. Appl. Math.*, **26** (2015), 143–173. https://doi.org/10.1017/S0956792514000370

3. D. Lacitignola, B. Bozzini, R. Peipmann, I. Sgura, Cross-diffusion effects on a morphochemical model for electrodeposition, *Appl. Math. Model.*, **57** (2018), 492–513. https://doi.org/10.1016/j.apm.2018.01.005

4. D. Lacitignola, B. Bozzini, M. Frittelli, I. Sgura, Turing pattern formation on the sphere for a morphochemical reaction-diffusion model for electrodeposition, *Commun. Nonlinear Sci. Numer. Simulat.*, **48** (2017), 484–508. https://doi.org/10.1016/j.cnsns.2017.01.008

5. D. Lacitignola, I. Sgura, B. Bozzini, T. Dobrovolska, I. Krastev, Spiral waves on the sphere for an alloy electrodeposition model, *Commun. Nonlinear Sci. Numer. Simulat.*, **79** (2019), 104930. https://doi.org/10.1016/j.cnsns.2019.104930

6. A. Madzvamuse, A. W. Chung, C. Venkataraman, Stability analysis and simulations of coupled bulk-surface reaction-diffusion systems, *Proc. R. Soc. A*, **471** (2015), 20140546. https://doi.org/10.1098/rspa.2014.0546

7. A. Madzvamuse, A. W. Chung, The bulk-surface finite element method for reaction-diffusion systems on stationary volumes, *Finite Elem. Anal. Des.*, **108** (2016), 9–21. https://doi.org/10.1016/j.finel.2015.09.002

8. M. Frittelli, A. Madzvamuse, I. Sgura, The bulk-surface virtual element method for reaction-diffusion PDEs: analysis and applications, *Commun. Comput. Phys.*, **33** (2023), 733–763. https://doi.org/10.4208/cicp.OA-2022-0204

9. P. Hansbo, M. G. Larson, S. Zahedi, A cut finite element method for coupled bulk-surface problems on time-dependent domains, *Comput. Meth. Appl. Math.*, **307** (2016), 96–116. https://doi.org/10.1016/j.cma.2016.04.012

10. K. Deckelnick, C. M. Elliott, T. Ranner, Unfitted finite element methods using bulk meshes for surface partial differential equations, *SIAM J. Numer. Anal.*, **52** (2014), 2137–2162. https://doi.org/10.1137/130948641

11. M. Cheng, L. Ling, Kernel-based meshless collocation methods for solving coupled bulk-surface partial differential equations, *J. Sci. Comput.*, **81** (2019), 375–391. https://doi.org/10.1007/s10915-019-01020-2

12. M. Frittelli, I. Sgura, Matrix-oriented FEM formulation for reaction-diffusion PDEs on a large class of 2D domains, *Appl. Numer. Math.*, 2023. https://doi.org/10.1016/j.apnum.2023.07.010

13. V. Simoncini, Computational methods for linear matrix equations, *SIAM Rev.*, **58** (2016), 377–441. https://doi.org/10.1137/130912839

14. M. Frittelli, A. Madzvamuse, I. Sgura, Virtual element method for elliptic bulk-surface PDEs in three space dimensions, *Numer. Methods Partial Differ. Equations*, **39** (2023), 4221–4247. https://doi.org/10.1002/num.23040

15. I. Sgura, A. S. Lawless, B. Bozzini, Parameter estimation for a morphochemical reaction-diffusion model of electrochemical pattern formation, *Inverse Probl. Sci. Eng.*, **27** (2019), 618–647. https://doi.org/10.1080/17415977.2018.1490278

16. I. Sgura, L. Mainetti, F. Negro, M. G. Quarta, B. Bozzini, Deep-learning based parameter identification enables rationalization of battery material evolution in complex electrochemical systems, *J. Comput. Sci.*, **66** (2023), 101900. https://doi.org/10.1016/j.jocs.2022.101900

17. A. Quarteroni, *Numerical models for differential problems*, Milano: Springer, 2009. https://doi.org/10.1007/978-88-470-1071-0

18. J. Smoller, *Shock waves and reaction-diffusion equations*, New York: Springer, 1994. https://doi.org/10.1007/978-1-4612-0873-0

19. B. Ahmad, A. Alsaedi, F. Brezzi, L. D. Marini, A. Russo, Equivalent projectors for virtual element methods, *Comput. Math. Appl.*, **66** (2013), 376–391. https://doi.org/10.1016/j.camwa.2013.05.015

20. L. Mascotto, The role of stabilization in the virtual element method: a survey, *Comput. Math. Appl.*, **151** (2023), 244–251. https://doi.org/10.1016/j.camwa.2023.09.045

21. L. Beirão da Veiga, F. Brezzi, L. D. Marini, A. Russo, The Hitchhiker's guide to the virtual element method, *Math. Mod. Meth. Appl. Sci.*, **24** (2014), 1541–1573. https://doi.org/10.1142/S021820251440003X

22. M. Frittelli, A. Madzvamuse, I. Sgura, C. Venkataraman, Preserving invariance properties of reaction-diffusion systems on stationary surfaces, *IMA J. Numer. Anal.*, **39** (2019), 235–270. https://doi.org/10.1093/imanum/drx058

23. A. Kazarnikov, H. Haario, Statistical approach for parameter identification by Turing patterns, *J. Theor. Biol.*, **501** (2020), 110319. https://doi.org/10.1016/j.jtbi.2020.110319

24. M. C. D'Autilia, I. Sgura, V. Simoncini, Matrix-oriented discretization methods for reaction-diffusion PDEs: comparisons and applications, *Comput. Math. Appl.*, **79** (2020), 2067–2085. https://doi.org/10.1016/j.camwa.2019.10.020

25. I. Sgura, B. Bozzini, D. Lacitignola, Numerical approximation of Turing patterns in electrodeposition by ADI methods, *J. Comput. Appl. Math.*, **236** (2012), 4132–4147. https://doi.org/10.1016/j.cam.2012.03.013